Ocean Dynamics (2003) 53: 27–51
DOI 10.1007/s10236-002-0022-7

**Emil V. Stanev · Jörg-Olaf Wolff · Hans Burchard
Karsten Bolding · Götz Flöser**

On the circulation in the East Frisian Wadden Sea: numerical modeling and data analysis

Received: 29 May 2002 / Accepted: 26 September 2002

Abstract In this paper we use a combination of numerical modeling and data analysis to gain a better understanding of the major characteristics of the circulation in the East Frisian Wadden Sea. In particular, we concentrate on the asymmetry of the tidal wave and its modulation in the coastal area, which results in a complex pattern of responses to the sea-level forcing from the North Sea. The numerical simulations are based on the 3-D primitive equation General Estuarine Transport Model (GETM) with a horizontal resolution of 200 m and terrain-following vertical coordinates. The model is forced at its open boundaries with sea-level data from an operational model for the German Bight (German Hydrographic Office). The validation data for our model simulations include time series of tidal gauge data and surface currents measured at a pile in the back-barrier basin of the Island Langeoog, as well as several ADCP transects in the Accumer Ee tidal inlet.

Circulation and turbulence characteristics are investigated for typical situations driven by spring and neap tides, and the analysis is focused on dominating temporal and spatial patterns. By investigating the response of five back-barrier basins with rather different morphologies to external forcing, an attempt is made to elucidate the dominating physical balances controlling the circulation in the individual sub-basins. It is demonstrated that the friction at the seabed tends to slow down the tidal signal in the shallow water. This leads to the establishment of flood dominance in the shallow sea north of the barrier islands. South of the islands, where the water volume of the channels at low tide is smaller than the tidal prism, the asymmetry of the tidal signal is shifted towards ebb dominance, a feature which is particularly pronounced at spring tide.

At the northern open boundary, the tidal wave propagating from west to east generates a sea-level difference of ~ 1 m along the boundary, and thereby triggers vigorous alongshore currents. The frictional control in the model is located in the inlets, as well as along the northern boundary. The correlation between velocity and turbulent kinetic energy tends to the establishment of a net southward transport, giving theoretical support to the observed accumulation of sediments on the intertidal flats. Weak turbulence along the northern shores of the barrier islands and the small magnitude of the residual currents there promote accumulation of suspended matter in these areas, although wave action will generally counteract this effect.

Keywords Wadden Sea · Tidal asymmetry · Energy dissipation · Regional numerical modeling · Validation against observations

Responsible Editor: Jean-Marie Beckers

E. V. Stanev (✉) · J.-O. Wolff
ICBM, Physical Oceanography (Theory),
University of Oldenburg,
Postfach 2503, 26111 Oldenburg, Germany
e-mail: e.stanev@icbm.de

H. Burchard
Baltic Sea Research Institute,
Warnemünde, Germany

K. Bolding
CEC-Joint Research Centre, Ispra, Italy

G. Flöser
Institute for Coastal Research,
GKSS Research Centre, Geesthacht, Germany

1 Introduction

The East Frisian Wadden Sea is a narrow tidal water body between the Ems river mouth in the west, the Jade Channel in the east, a chain of barrier islands in the north, and the German coast in the south (see Fig. 1 for a general overview of the area of interest). The narrow tidal inlets act as perforations in the shoreline through which North Sea water is imported into the shallow tidal basins (colored yellow in Fig. 1) during the flooding period. During the ebb phase of the tide, the waters accumulated in the back-barrier basins flow back into the North Sea through the inlets. Under the dominating influence of tides, wind, and wind waves, a specific

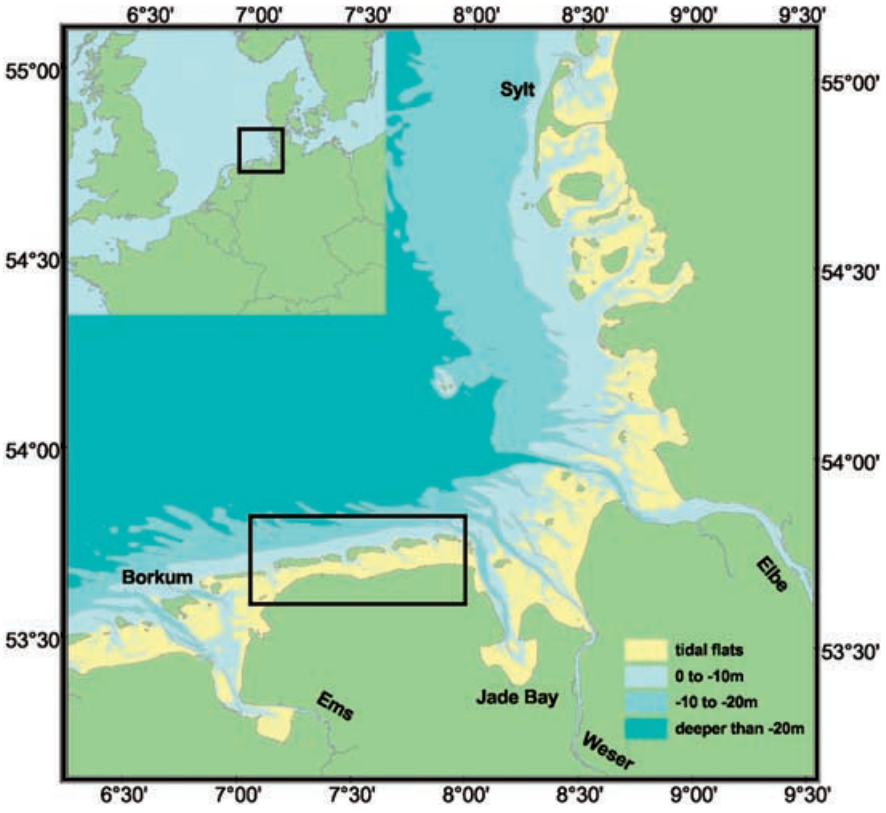

Fig. 1 The North Sea, German Bight (in the *square frame on the inset*) and the East Frisian Wadden Sea (in the *rectangle frame*). The plotted depths are negative. The yellow color gives approximately the areas which could become dry. In the adjacent area (lightest blue) the depth is less than 10 m (see legend), but this area cannot become dry

coastal water mass is formed which is rich in nutrients and suspended particulate matter, thereby supporting a diverse flora and fauna. This water mass is periodically exposed to mixing with North Sea waters (during flood), and is partially exported back into the North Sea (during ebb). In this way, the Wadden Sea acts as a buffer zone between ocean and land.

The East Frisian Wadden Sea plays a key role in the coastal/open-ocean exchange and is therefore subject to strong environmental concerns and considerable research interests. Even though the number of recent studies has substantially extended the understanding of its complex behavior (see, e.g. Dittmann 1999 and the references therein), much remains to be learned about the physical balances. Sea-level measurements from tide gauge stations are the only long-term observations of physical quantities available in the East Frisian Wadden Sea. Observations of other physical parameters, like temperature, salinity, or even currents, are sparse in either time or space. The construction of a reliable circulation pattern in this area and the understanding of its spatial and temporal variability is therefore still a challenging task.

The tidal inlets are the dynamically most active part of the Wadden Sea, linking the processes on the intertidal flats to the forcing factors originating from the North Sea. The important role of tidal inlets as waterways with intense naval traffic and their vulnerability to sedimentation has motivated numerous studies on physical and engineering aspects of their dynamics (comprehensive reviews are given by Keulegan 1967; Lighthill 1978; Mehta 1978; Trowbridge et al. 1998).

A first-order description of a simple inlet–bay system (Fig. 2) can be based on the following system of differential equations for the sea surface elevation in the bay ζ and a current with velocity u through the inlet,

$$\frac{\mathrm{d}u}{\mathrm{d}t} = \frac{g}{L_c}(\zeta_0 - \zeta) - \gamma|u|u \tag{1}$$

$$\frac{\mathrm{d}\zeta}{\mathrm{d}t} = \frac{A_c}{A_b}u \ , \tag{2}$$

where g is the acceleration due to gravity, A_c and L_c the cross-sectional area of the inlet (or channel) and its length, respectively (the index c stands for channel), A_b the area of the bay (index b), and γ is a friction parameter. Equations (1) and (2) lead to a second-order differential equation for ζ (like a damped harmonic

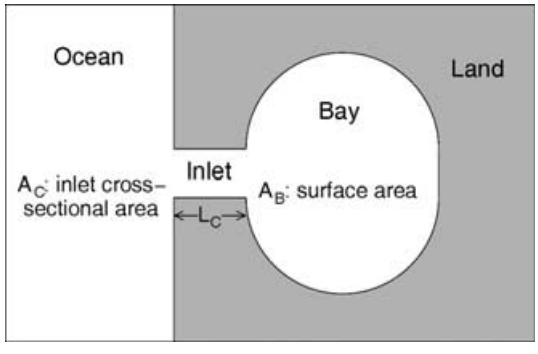

Fig. 2 Schematic representation of the system ocean–inlet–bay–land

oscillator) forced by sea-surface oscillations in the open ocean ζ_0:

$$\frac{\mathrm{d}^2\zeta}{\mathrm{d}t^2}+\gamma\frac{A_b}{A_c}\left|\frac{\mathrm{d}\zeta}{\mathrm{d}t}\right|\frac{\mathrm{d}\zeta}{\mathrm{d}t}+g\frac{A_c}{A_bL_c}\zeta=g\frac{A_c}{A_bL_c}\zeta_0\ . \tag{3}$$

The solution of this equation is known as the Helmholtz mode (Lighthill 1978) and describes the adjustment of the sea-level elevation in the bay to the external forcing. It gives a first-order estimate of the sea-level oscillation in real bays as well as the transport through a real inlet.

However, the simplifications under which Eqs. (1) to (3) are formulated are severe, and include, amongst others, the following: vertical walls instead of sloping banks in the inlet and bay, no frictional dissipation in the open ocean and bay, a small tidal range compared to the mean water depth, and a horizontal sea level in the bay at all times. Although similar equations have been widely used in coastal engineering, they can hardly describe the complete dynamics of real systems. Indeed, none of these assumptions is strictly justified in the case of the East Frisian Wadden Sea.

Numerical models, on the other hand, though more difficult to use, give a more realistic picture of the behaviour of the coupled coastal-open ocean system, and numerous simulations of estuarine systems in the world have been carried out. Of particular interest is the modelling expertise gained in the neighbouring areas of the Dutch Wadden Sea (Ridderinkhof 1988; Ridderinkhof and Zimmerman 1990a,b) and in the North Frisian Wadden Sea (Dick and Schönfeld 1996). Currently, numerical models of different complexity are applied when studying sedimentation dynamics and morphological evolution of Wadden Sea (van der Ham and Winterwerp 2001; de Kok 2002; de Swart et al., personal communication).

To our knowlege, the East Frisian Wadden Sea has so far been subject to numerical simulations only in an earlier study by Hübner and Backhaus (1997) using the Hamburg Watten Meer Model (HAWAM, see Backhaus 1983) which is a non-linear two-dimensional barotropic model. Simulations in some local areas (Jade–Weser Estuary) have been carried out by the Coastal Division of the German Federal Waterways Engineering and Research Institute, Hamburg.

Our major motivation here is to present results from the General Estuarine Transport Model (GETM) of Burchard and Bolding (2002) for a typical system of mixed estuaries. The comparison of the simulations with the observations is very promising and motivates us to further analyze the model data in order to derive new information about the governing dynamics. The paper is structured as follows: we first describe the model and its setup for the region of the East Frisian Wadden Sea, including a discussion of the forcing at the open boundaries, then we compare our simulations with available observations. After having established the performance of the model, we describe various model characteristics which are not currently accessible to direct measurements: turbulent kinetic energy and its dissipation rate, area mean properties in several tidal basins.

2 The general estuarine transport model (GETM)

2.1 Hydrodynamic equations

In this section we discuss the model setup and the major characteristics of the model relevant to the physical conditions in the study area. A more detailed description of the numerical model can be found in a technical report by Burchard and Bolding (2002). The momentum equations in Cartesian coordinates read:

$$\frac{\partial u}{\partial t}+\alpha\left[\frac{\partial(u^2)}{\partial x}+\frac{\partial(uv)}{\partial y}-fv+\frac{\partial(uw)}{\partial z}\right]=-g\frac{\partial\zeta}{\partial x}+\frac{\partial}{\partial z}\left(A_V\frac{\partial u}{\partial z}\right)+A_H\nabla^2u \tag{4}$$

$$\frac{\partial v}{\partial t}+\alpha\left[\frac{\partial(uv)}{\partial x}+\frac{\partial(v^2)}{\partial y}+fu+\frac{\partial(vw)}{\partial z}\right]=-g\frac{\partial\zeta}{\partial y}+\frac{\partial}{\partial z}\left(A_V\frac{\partial v}{\partial z}\right)+A_H\nabla^2v \tag{5}$$

$$\frac{\partial u}{\partial x}+\frac{\partial v}{\partial y}+\frac{\partial w}{\partial z}=0\ . \tag{6}$$

Most of the above notations are standard, where u, v, and w are the velocity components with respect to the x (east), y (north), and z (upward) direction, respectively, f is the Coriolis parameter, g is the acceleration due to gravity, and ζ is the sea-surface height. The lateral eddy viscosity $A_H(x,y)$ has been introduced to suppress non-physical noise along the open boundaries in a three-grid-point-wide sponge layer, where it changes exponentially from its boundary value of $10^3\,\mathrm{m^2s^{-1}}$ to $1/e$ of this value. In the interior of our model domain, which has a mean depth of less than 10 m, the dissipation is dominated by vertical friction. $A_V(k,\varepsilon,\alpha)$ is a generalized form of the vertical eddy viscosity coefficient, k the turbulent kinetic energy (TKE) per unit mass, ε the eddy dissipation rate (EDR) of kinetic energy due to viscosity, and α a non-dimensional number reducing the influence of some terms in these equations in situations of very thin fluid coverage on the intertidal flats. This process of drying and flooding is incorporated in the hydrodynamical equations through a parameter α which equals unity in regions where a critical water depth D_{crit} is exceeded and which approaches zero when the thickness of the water column $D=H+\zeta$ tends to a minimum value D_{min}:

$$\alpha=\min\left(1,\frac{D-D_{\mathrm{min}}}{D_{\mathrm{crit}}-D_{\mathrm{min}}}\right)\ , \tag{7}$$

where H is the constant over time local depth, taken as the bottom depth below mean sea level in the model area. In our model simulations, the minimum allowable

thickness $D_{\min}$ of the water column is 2 cm and the critical thickness D_{crit} is 10 cm. For a water depth greater than 10 cm ($D \geq D_{\text{crit}}$ and $\alpha = 1$), the full physics are included. In the range between critical and minimal thickness (between 10 and 2 cm) the model physics are gradually switched towards friction domination, i.e., by reducing the effects of horizontal advection and Coriolis acceleration in Eqs. (4) and (5) and varying the vertical eddy viscosity coefficient A_V according to

$$A_V = \nu_t + (1-\alpha)\nu_\alpha \ , \tag{8}$$

where $\nu_\alpha = 10^{-1}\text{m}^2\text{s}^{-2}$ is a constant background viscosity and the eddy viscosity ν_t is obtained from the relation

$$\nu_t = c_\mu^4 \frac{k^2}{\varepsilon} \ , \tag{9}$$

with $c_\mu = 0.56$ (see, e.g., Rodi 1980).

In GETM, the momentum Eqs. (4) and (5) and the continuity Eq. (6) are supplemented by a pair of equations describing the time evolution of the turbulent kinetic energy k and its dissipation rate ε:

$$\frac{\partial k}{\partial t} - \frac{\partial}{\partial z}\left(\frac{\nu_t}{\sigma_k}\frac{\partial k}{\partial z}\right) = P - \varepsilon \tag{10}$$

$$\frac{\partial \varepsilon}{\partial t} - \frac{\partial}{\partial z}\left(\frac{\nu_t}{\sigma_\varepsilon}\frac{\partial \varepsilon}{\partial z}\right) = \frac{\varepsilon}{k}(c_1 P - c_2 \varepsilon) \ , \tag{11}$$

where σ_k and σ_ε are the turbulent Schmidt numbers which are specified as follows. In order to be consistent with the profiles in the logarithmic layer (the near-boundary layer where the vertical turbulent stress is assumed to be constant) σ_ε has to have the form:

$$\sigma_\varepsilon = \frac{\kappa^2}{c_\mu^2(c_2 - c_1)} \ , \tag{12}$$

where κ is the von Karman constant, $c_1 = 1.44$, and $c_2 = 1.92$ (see, e.g. Rodi 1980). The turbulent Schmidt number, σ_k, is set to the traditional value of unity (see Rodi 1980).

The vertical shear production P is a function of the shear frequency S:

$$P = \nu_t S^2 \tag{13}$$

with

$$S^2 = \left(\frac{\partial u}{\partial z}\right)^2 + \left(\frac{\partial v}{\partial z}\right)^2 \ . \tag{14}$$

2.2 Bottom and surface boundary layers

An important physical characteristic of the coastal area is that the density in the water column (contrary to the open ocean) is vertically well mixed, the mixing coefficient reaching its maximum value approximately halfway from the bottom to the sea surface. This is to be expected because the size of the eddies increases with increasing distance from the boundaries. Because the Wadden Sea undergoes continuous flooding and drying the vertical boundaries (sea surface and bottom) are very close to each other and the physical processes describing boundary layer evolution have to be considered in great detail. In fact, the dominating balance in the Wadden Sea is between forcing at the sea surface and open boundaries (mainly tides and wind), and dissipation of momentum at the sea floor. The success of the model depends on a detailed description of the physical processes in the boundary layers and their resolution.

The primary forcing in the Wadden Sea is generated by tidal oscillations and we thus concentrated our study on the effects of this forcing mechanism. The rise and fall of the tides creates horizontal pressure gradients which result in currents. Currents reach maximum values near the surface and tend to decrease with depth. There is clear observational evidence that the velocity profiles close to the bottom in the East Frisian Wadden Sea can be adequately described by a logarithmic boundary layer (Davis and Flemming 1991; Antia 1993):

$$\frac{u}{u_*^b} = \frac{1}{\kappa} ln\left(\frac{z + z_0}{z_0}\right) \ , \tag{15}$$

where $u_*^b = \sqrt{\tau_b}$ is the friction velocity at the sea floor, $\tau_b = \nu_t(\partial u/\partial z)$ is the bed shear stress and z_0 is the bottom roughness length. As we ignore the effects of wind stress in this study, the dynamic boundary conditions at the sea surface $z = \zeta$ are given by :

$$\tau_\zeta = 0 \ . \tag{16}$$

Boundary conditions for the turbulent kinetic energy k and dissipation rate ε are also required. For k we apply a zero vertical flux condition at the sea surface. The bottom boundary condition uses the bed shear stress in the logarithmic layer (Eq. 15). The details about the implementation of this boundary condition in the discrete space of the model are given in Section 2.3 (see Eq. 25).

The boundary values for ε are calculated using the following relationship for the macro length scale of turbulence:

$$L = c_\mu^{3/4} \frac{k^{3/2}}{\varepsilon} \ . \tag{17}$$

Equation (17) describes the size of the energy containing turbulent eddies as a function of k and ε.

Parameterizing the length scales as proportional to the surface $z_0|_\zeta$ and bottom $z_0|_{-H}$ roughness lengths, respectively

$$L_\zeta = \kappa z_0\Big|_\zeta \tag{18}$$

and

$$L_{-H} = \kappa z_0\Big|_{-H} \tag{19}$$

leads to boundary conditions for ε at the surface ($z = \zeta$)

$$\varepsilon_\zeta = c_\mu^{3/4} \frac{k^{3/2}}{L_\zeta} \tag{20}$$

and the bottom ($z = -H$)

$$\varepsilon_{-H} = c_\mu^{3/4} \frac{k^{3/2}}{L_{-H}} \quad . \tag{21}$$

The bottom roughness length is approximately 0.03 times the height of the roughness elements (see e.g., Kagan 1995) and is here set to 10^{-3} m. The surface roughness scale is 10^{-1} m.

This type of boundary condition (no flux for k and k dependence for ε) has been suggested by Burchard and Petersen (1999). It is a formulation of the law of the wall (see Eq. 15), which also works at the surface of wind-free open channel flow. In contrast to this, classical formulations using the surface friction velocity u_*^s, which is zero here, fail in such situations.

2.3 Discretization

The model uses terrain-following vertical coordinates. The vertical column extending from the bottom $-H(x,y)$ to the surface $\zeta(x,y,t)$ is divided into N nonintersecting layers h_k (see Fig. 3a), $k = 1,\ldots,N$ by introducing internal surfaces z_k, $k = 1,\ldots,N-1$, each depending on the horizontal position (x,y). In the case of equidistant $\sigma-$coordinates used in the present model, the thicknesses of model layers are

$$h_k = \frac{D}{N} \tag{22}$$

for $1 \le k \le N$.

The transformation of the finite difference equations into $\sigma-$ coordinates is described in detail in the technical report of Burchard and Bolding (2002).

The vertically staggered grid (Fig. 3a) includes control volumes around pressure or tracer grid points. The vertical velocity points are above and below the tracer points, and are also the grid points where the turbulent quantities k, ε, and ν_t are computed.

The vertical discretization of our model consists of ten layers. Because the sea-level height changes continuously during the model integration, and because the thickness of the water column D is a function of sea level, the vertical discretization (see Eq. 22) changes with time. In our model area the coarsest resolution (in the deepest channels) is ~ 2 m. In the limiting case when the thickness of water column is $D_{\min}$ the resolution is ~ 2 mm. The dependence of the layer thickness on the local sea level is quite important, because in large areas of our model domain the water depth becomes comparable with the tidal range.

In the horizontal, the grid is a staggered Arakawa-C grid (Arakawa and Lamb 1977) where the positions of the u points are west and east, and the positions of the v points are south and north of the pressure point (Fig. 3b). In the present version of the model, an upstream advection scheme is used when solving momentum equations.

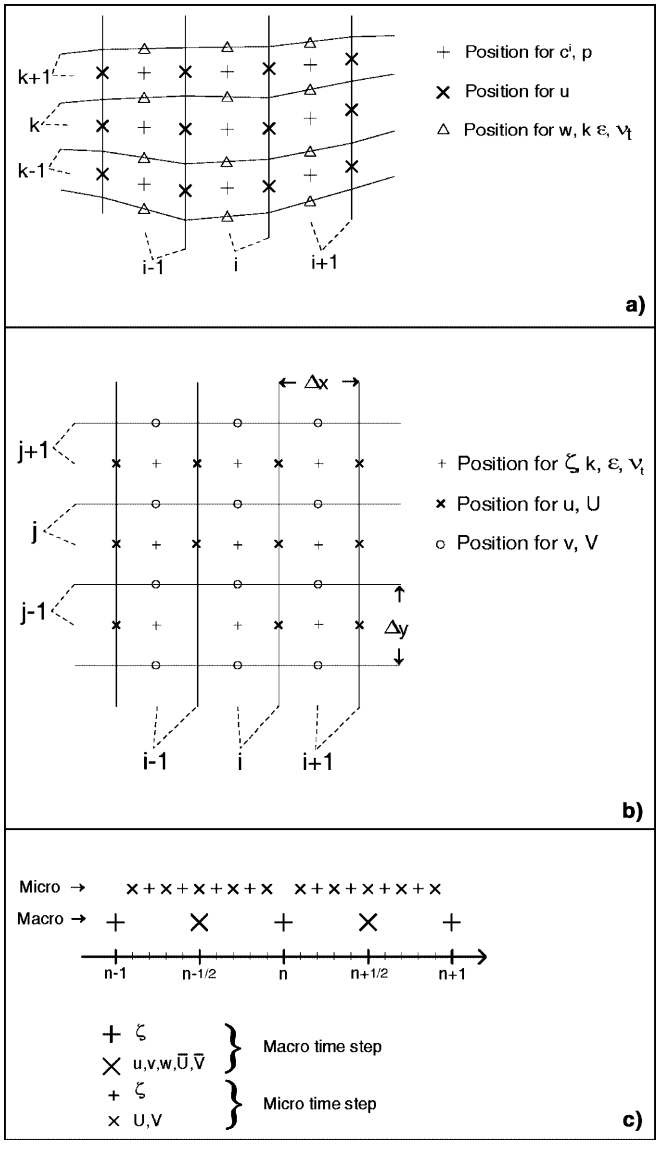

Fig. 3a–c The model grid. **a** Vertical discretization. **b** Horizontal discretization and **c** Time discretization showing the time-stepping technique using micro and macro time steps (see for the definitions Eqs. 23, 24). Most of notations are explained in the text, c^i and p denote tracer and pressure, $\bar{U}, \bar{V}$ are averaged during the macro time step barotropic velocities

An efficient algorithm to solve the system of governing equations is obtained by splitting the solution into an internal and external mode. The latter is represented by the system of shallow-water equations derived from Eqs. (4), (5) and (6). A detailed description of the equations and their discretization in time and space is given by Burchard and Bolding (2002). Advection in the internal and the external mode is treated explicitly, whereas vertical diffusion of all variables is treated implicitly, which leads to tri-diagonal linear systems in the vertical. The explicit treatment of advection introduces a time step constraint for the external mode through the speed of surface gravity waves (Beckers and Deleersnijder 1993):

$$\Delta t \leq \frac{1}{\sqrt{2gH}\sqrt{\frac{1}{\Delta x^2}+\frac{1}{\Delta y^2}}} \quad . \tag{23}$$

In contrast to this, the time step of the internal system is dictated by the usually much smaller current velocities,

$$\Delta t_{int} < \min\left\{\frac{\Delta x}{u_{\max}}, \frac{\Delta y}{v_{\max}}\right\} \quad , \tag{24}$$

which in the case of subcritical flow is a much weaker constraint. The time discretization therefore includes different time steps for the internal (macro times steps Δt_{int}) and external (micro time steps Δt_{ext}) mode, and Δt_{ext} is an integer fraction M of the macro time step Δt_{int}. The time-stepping principle is shown in Fig. 3c.

Some of the subgrid parameterizations could depend on the vertical discretization, as is the case with the bed shear stress. In the model we cannot simply set the lowermost velocity to zero. This would be physically correct for a point directly at the bed, but the lack of resolution in some locations precludes this possibility. To solve this problem, we assume that the lowermost grid box is fully submerged within the logarithmic boundary layer. This does not mean that we directly trigger a log layer in the whole water column, but only that

$$u_1 = \frac{u_*^b}{\kappa} ln\left(\frac{0.5h_1 + z_0}{z_0}\right) \quad , \tag{25}$$

where h_1, u_1 are the thickness and velocity of the deepest box, respectively.

Because our model resolution of 200 m is the same as that in the study of the Sylt–Rømø basin by Burchard (1998), we use basically the same parameter settings and refer to that study for a discussion of the sensitivity of the model to changes in these parameters. Given the resolution, we are constrained to a macro time step Δt_{int} of 15 s and a micro time step Δt_{ext} of 3 s.

3 The model area

3.1 General characteristics

The German Wadden Sea comprises the nearshore zone of the German Bight (Fig. 1). The tidal range varies from ~ 2.5 m (Islands Borkum and Sylt) to ~ 3.5 m (the Elbe river mouth) and, according to the classification of Hayes (1979), this region is exposed to upper mesotidal conditions. The existing literature addressing the dynamics in this area is quite large, but most of the papers either give a rather general view on currents and sea-level variability in the coastal zone (e.g., Otto et al. 1990), or are mainly based on local nearshore measurements (e.g., Lassen and Siefert 1991).

The characteristic temporal and spatial patterns of sea-surface elevation and currents in the Wadden Sea can only be adequately understood by resolving the relevant scales in time and space.

The model area is concentrated on the waters around the chain of barrier islands shown in the area bounded by the rectangular frame in Fig. 1. The yellow areas are prone to drying and flooding. A major portion of the model area is thus periodically flooded by the tides and small-scale morphological features (e.g. narrow channels) crucially dominate the physical processes.

With a horizontal resolution of 200 m, the topography of the model domain is more clearly identified in Fig. 4a. This map was computed from a dataset with 50 m resolution using detailed topographic maps from the past two decades. The chosen resolution is, in our opinion, the coarsest one which can still well resolve the important topographic features of the East Frisian Wadden Sea. One important consideration to chose this resolution was that the inlets between the islands, which are the most energetically active areas in the model domain, are resolved with at least several grid points (five points in the narrowest inlet, the Wichter Ee, and more than ten points in the rest of the inlets).

In order to reduce the number of land points in the model area, we rotated the region bounded by the rectangular frame in Fig. 1 by $\sim 9°$ (see the arrow pointing to the north in Fig. 4). Because our interest is primarily focused on the medium-sized and small tidal basins (south of the line connecting the islands Norderney to Wangerooge), we excluded the westernmost part of the East Frisian Wadden Sea (i.e. the area around the islands of Borkum and Juist), as well as the embayment of the Jade and Weser estuary in the east (cf. Fig. 4 with Fig. 1).

In Fig. 4b we have indicated the geographical names of the islands and inlets which are referred to in the paper. In the upper panel of the same figure one can distinguish the typical morphological features which are observed in mesotidal basins: barrier islands, tidal inlets with openings varying from 1 to 3 km, tidal channels, tidal deltas, and tidal flats. There are seven inlets altogether in the model area. Each of these connects one tidal basin with the open sea. The inlet of Norderney (Norderney Seegat) actually consists of two channels, and we therefore define two tidal basins to the south of it. This peculiarity is due to the complex bathymetry of the region, where the intertidal flats south of the Norderney Seegat are separated into two weakly connected basins.

The color coding in Fig. 4b distinguishes seven tidal basins connected to the North Sea. The horizontal extent of each basin has been defined by the waters coming in during an assumed constant flooding (in space) from its connecting inlet to the North Sea. Where the waters from two adjacent inlets meet, a watershed is defined and the boundary is fixed at that point. The boundaries between the tidal basins defined in this way roughly correspond to the boundaries of minimum water exchange specified in earlier studies (e.g. Flemming and Davis 1994).

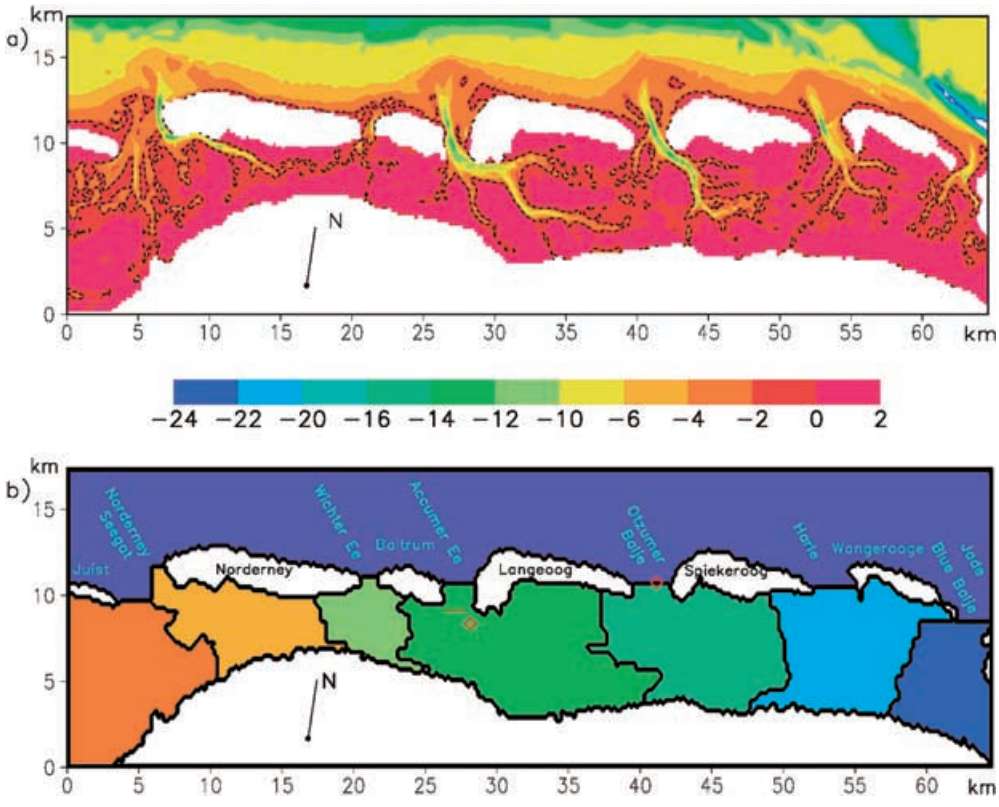

Fig. 4 **a** Topography of East Frisian Wadden Sea. The isobaths are represented as negative numbers (*m*) below the mean sea level. The *dashed isoline* contours the depth 1.6 m below mean sea level, which is approximately equal to the amplitude of spring tide. It thus specifies the areas which never dry during mean spring tide. The position of zero depth (in the figure the mean sea level) is calibrated in a way that the calculated changes in the volumes of individual basins are consistent with those existing in the literature data obtained from observations (e.g. Ferk 1995). **b** Individual tidal basins. The *diamond symbols* give the locations where we analyze data from observations and simulations (see further in text). The *short red line* in Accumer Ee gives the approximate position where ADCP sections have been carried out and observations are used for model validation

3.2 The impact of topography on tidal dynamics: first-order theoretical estimates

Being based on topography only, the regionalization in Fig. 4b is not unique because it is assumed that the tide is uniform over the entire area; the morphological characteristics of the individual tidal basins, which are summarized in Tables 1 and 2, may be subject to small uncertainties. Nevertheless, they support some earlier estimates for the region (e.g. Ferk 1995) and can thus be considered as a first-order generalization.

The generalized morphological characteristics of the tidal basins are given separately in Tables 1 and 2 for neap and spring tide conditions. This distinction is important because under the two different situations the physical balances differ substantially. The model area is an extremely shallow area where the volume of the tidal prism $\Delta V = V_h - V_l$, i.e. the difference between the volumes for high (V_h) and low (V_l) waters substantially exceeds the volume of water which remains in the basin during low tide (V_l). In most of model subareas the depth is shallower than the tidal range, which demonstrates that the storage capabilities of flat areas are much smaller than in the model domain north of the barrier islands (area NS in Tables 1 and 2), for instance. This specific topography is very important for the understanding of the governing physics, therefore we will briefly outline several important aspects of the tidal distortion in nearshore areas following the synthesis of Friedrichs and Aubrey (1988).

Table 1 Volumes, areas, mean depths and tidal prism under spring tide conditions for the tidal basins defined in Fig. 4b. The *abbreviations in the first row* correspond to the names of the island behind which the corresponding tidal basin is located. The abbreviation *MO* stands for Minsener Oog (the small island on the eastern boundary of the model area identifying the easternmost tidal basin. *NS* denotes the part of the North Sea that is covered by our model grid (see the regional mask in Fig. 4b). A_h and A_l are the surface areas corresponding to V_h and V_l. The mean depth H_m is given for high water (1.7 m). The *sixth row* shows the ratio between the tidal prism $\Delta V = V_h - V_l$ and the volume of water deeper than 1.7 m below the mean sea level, and the *last row* is the forcing term (see text)

	Ju	No	Ba	La	Sp	Wa	MO	NS
V_h (10^6 m^3)	167	114	42	231	184	142	89	3380
V_l (10^6 m^3)	14	28	3	57	39	19	10	2117
A_h (10^6 m^2)	71	42	22	91	71	66	39	378
A_l (10^6 m^2)	13	9	2	19	14	10	6	351
H_m(m)	2.37	2.70	1.88	2.53	2.59	2.18	2.27	8.90
$\Delta V/V_l$	10.4	3.1	12.1	3.1	3.7	6.7	7.8	0.6
rA_l/V_l	1.4	1.3	1.8	1.3	1.3	1.6	1.5	0.4

Table 2 As in Table 1, but for the neap tide. The tidal range is now 2.4 m and the high water level is 1.2 m

	Ju	No	Ba	La	Sp	Wa	MO	NS
V_h (10^6 m^3)	132	94	31	186	150	110	70	3190
V_l (10^6 m^3)	23	33	0.5	67	47	26	14	2295
A_h (10^6 m^2)	70	40	22	87	68	64	39	379
A_l (10^6 m^2)	22	12	4	24	20	15	10	362
H_m (m)	1.88	2.31	1.42	2.14	2.19	1.73	1.79	8.41
$\Delta V/V_l$	4.7	1.8	5.5	1.8	2.2	3.5	4	0.4
rA_l/V_l	1.3	1.1	1.7	1.1	1.1	1.4	1.3	0.3

The response of tidal basins to oceanic forcing is governed by three important parameters: (1) the volume of water which is exchanged between the basin and the open ocean during one tidal period, i.e. the tidal prism ΔV, (2) the volume of water which always remains in the tidal basins, i.e. the volume of deep channels below the low water level V_l, and (3) the external forcing measured by the tidal range $r = 2a$, where a is the tidal amplitude. In order to use comparable numbers we will multiply r by the surface area of deep channels at low water (i.e. by the numbers given in the fourth line of Tables 1 and 2). We consider V_l as the reference volume because that is the water which resides in the tidal basins. According to the concepts developed by Boon and Byrne (1981) and Fitzgerald and Nummedal (1983) (see also Friedrichs and Aubrey 1988), the ratio between the tidal prism and the reference volume, on one hand, and the forcing term and reference number, on the other, permits first-order estimates about the dominating dynamics in tidal basins.

The numbers in the last lines of Tables 1 and 2 measure the relative shallowness of the channel in comparison to the tidal range, and can be viewed as barotropic Froude numbers (Jay and Smith 1988). These numbers are usually larger than unity in the tidal basins of our model area. However, the Froude number is also high (~ 0.5) in the region NS, which is clear evidence for the fact that friction plays an important role in the entire model area. The impact of friction on the dynamics in the model area is controlled by the thickness of the water column, the latter being subject to tidal oscillations. Because friction is greater in shallow water, flow deceleration is stronger during the ebb tide. As a result, stronger currents occur during the flood phase and weaker currents during the ebb phase. Correspondingly, due to the law of mass conservation, the duration of the ebb phase is longer than that of the flood phase. This asymmetry, which governs the model physics in area NS, is known as flood dominance.

The major difference between NS and all other areas is that in the latter the ratio $\Delta V/V_l$ is much larger than unity. This means that the water exchanged between the North Sea and the tidal basin is higher than the amount of water which resides in the basin. In similar settings, the export and import of waters through the inlets may have different characteristic times, depending on the ratio between the maximum storage capacity of the basin ($\sim A_h$) and the water permanently stored in it ($\sim A_l$). This difference is well illustrated when comparing the third and fourth lines of Tables 1 and 2. Note that only in the area NS and the two numbers almost equal.

The physical control of $\Delta V/V_l$ can be roughly explained by Eq. (2). However, we have to keep in mind that in realistic bays: (1) the area A_b is different under high (A_h) and low (A_l) water (for the physical consequences of this, see Maas 1998), and (2) the definition of L_c is not quite clear. Nevertheless, it is obvious that around high water the wetted basin area is several times larger than around low water (compare the third and fourth lines in the tables), the number A_c/A_b thus becoming small. This ratio controls the speed of adjustment of the sea surface in the bay to the oscillations in the open sea (see Eq. 3), thus we can expect situations when symmetric oceanic forcing could trigger an asymmetric response. The adjustment is thus more rapid at low tide because the characteristic time $\sqrt{\frac{A_b}{A_c}\frac{L_c}{g}}$ is shorter. As shown by the data analysis done by Friedrichs and Aubrey (1988), as well as by their one-dimensional numerical experiments, in estuarine systems where the storage area largely exceeds the area of channels, the tidal curves in the bays are steeper and the currents are faster during the ebb phase. This situation is called ebb dominance. The analysis of the simulations produced by three-dimensional models is the next step towards a deeper understanding of the asymmetric response in our model area. This will be addressed in Section 7.

4 Model forcing and validation data

4.1 Data sources

Two types of data are used in the present study: forcing data and data which we use to validate the model. The first types of data are extracted from large-scale simulations, the second are from direct observations. In this section we describe these data and use them to characterize the oceanographic conditions in the model area.

Our model is a high-resolution regional ocean model, and as in all regional models, the quality of the simulations depends very much on the quality of the information provided at the boundaries. We have chosen sea-level data from the operational model of the German Federal Maritime and Hydrographic Agency (Bundesamt für Seeschiffahrt und Hydrographie, BSH) as boundary conditions for the regional model.

The BSH model is a three-dimensional prognostic model (Dick and Sötje 1990; Dick et al. 2001) which operates in two versions: (1) a coarse-resolution model including the North Sea and Baltic Sea (grid size is 10 km), and (2) a high-resolution model of the German Bight where the horizontal resolution is 1.8 km. The boundary conditions at the open boundaries are formulated using tidal values calculated from the tidal constituents of 14 partial tides. The model predicts currents, water level, water temperature, salinity, and ice coverage. At the sea surface the model is forced with meteorological and wave forecasts (wind, atmospheric pressure, wave characteristics, air temperature, specific humidity, and clouds), which are provided by the German Weather Service (Deutscher Wetterdienst, DWD).

Even though the BSH operational model is (to our knowledge) the model with the highest resolution operating in the region of the our interest, it obviously cannot sufficiently describe the local dynamics of the Wadden Sea. The tidal basins are resolved in the meridional direction by only one to three grid points, and

this results in a relatively noisy pattern during part of the tidal cycle (Fig. 5c). We recall here that the horizontal resolution of our regional model (200 m) is nine times finer than the resolution of the BSH model.

An excellent data source to compare simulated transports with observations was created in 2000 when the Institute for Coastal Research in the GKSS Research Centre, Geesthacht, Germany, initiated a long-lasting campaign including pile station measurements (10-min records) of sea level, currents and other hydrophysical and biogeochemical parameters of seawater, ADCP transects along and across the tidal channels, and other local observations. These data are described in more detail in Section 4.3.

4.2 Forcing (data from large-scale simulations)

4.2.1 Formulation of model boundary conditions

To illustrate the effect of the large-scale circulation on our regional model, we show the sea-level evolution from the BSH model during a spring tide cycle in a region which is $\sim$ four times larger than our model area. The sea-level patterns shown in Fig. 5 illustrate the general circulation regime in the southern part of the German Bight, the latter greatly affecting the dynamics in our model area. The local circulation is driven by the coastal wave associated with the well-known amphidromy at $\sim 55.5°$N, $\sim 5.5°$E. The dominant horizontal patterns are illustrated by the sea-surface anomaly, i.e. the difference between sea level and actual mean sea level

$$\Delta\zeta(x,y,t) = \zeta(x,y,t) - \frac{1}{area}\int\int \zeta(x,y,t)\; dx\; dy \;, \qquad (26)$$

where $area = \int\int dxdy$ is the basin area. Four phases of the tidal cycle are shown in Fig. 5: high-water HW, low-water LW, and the two intermediate phases (noted as EBB and FLOOD).

In the coastal area in front of the barrier islands, the slope of the sea level is steeper during the flood phase than during the ebb phase, which supports the results obtained by Lassen and Siefert (1991). The tidal range reaches maximum values in the south eastern corner of the area and decreases to the north and to the west (Fig. 5e), which also agrees with the estimates from tide gauge stations documented by the same authors.

In the following, we give a short introduction to the dynamics in the model area and the adjacent ocean based on an examination of Lagrangian trajectories. We released particles at the locations marked by the black symbols in Fig. 6 and propagated them for one (spring) tidal period with the surface velocity data from the BSH model. The magnitude of the tidal currents approaches 1 ms^{-1}, and the trajectories reveal that the mass transport is subject to a large asymmetry. The particles undergo

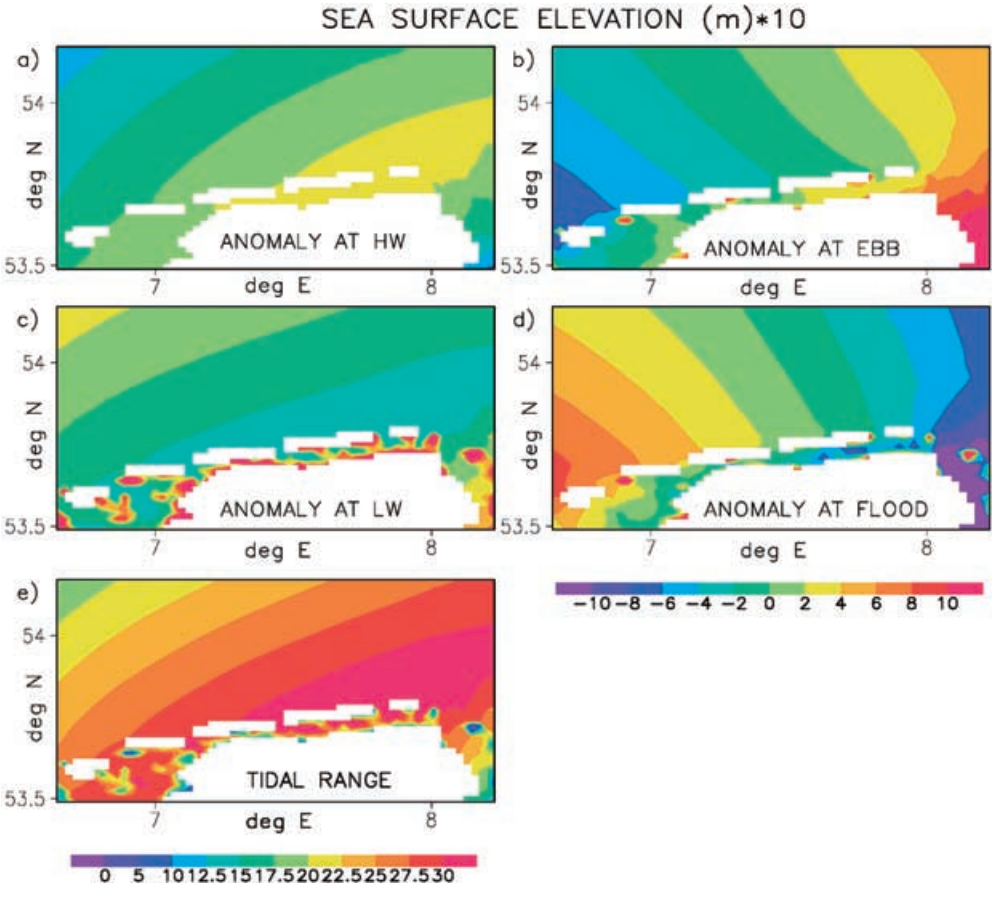

Fig. 5a–d Anomalies of sea level during one spring tide period (16 October 2000) computed from the output of the BSH operational model. The first panel **a** corresponds to high water (HW) which occurred on that day at 12:15 UTC. Every subsequent snapshot (*EBB, LW,* and *FLOOD*) is after 0.25 tidal period. **e** The tidal range. The data were kindly made available by S. Dick, BSH

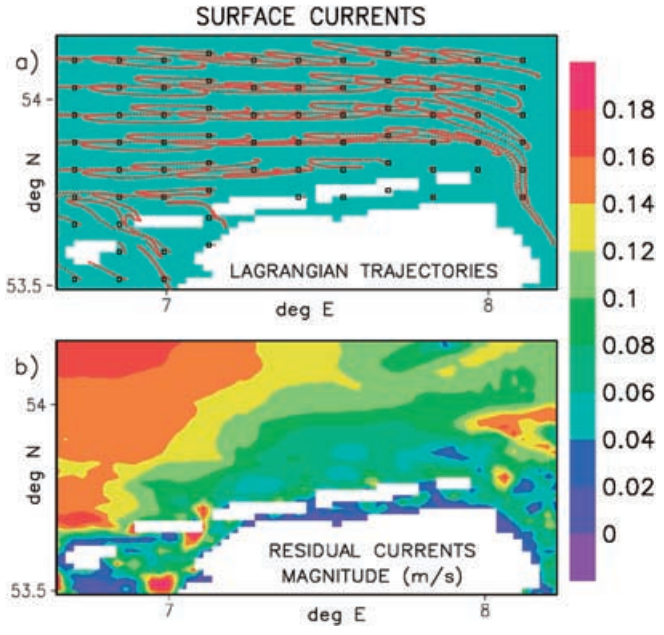

Fig. 6 a Lagrangian trajectories computed from surface currents simulated by the BSH operational model during a spring tide period (16 October 2000). The *black symbols* give the origin of the individual trajectories. **b** The magnitude of the residual currents

anticlockwise rotations strongly elongated along the isobaths. This is a typical behavior for the shallow region north of the barrier islands, where the depth does not exceed 20–30 m. The periodic displacement of water parcels during one tidal cycle reaches distances which are comparable to the horizontal scale of our regional model. This shows that the model is subject to a vigorous influence from the open ocean, and any error in the boundary forcing will have a strong influence on the model dynamics. Because we used sea-level information from the operational BSH model as the only external forcing, we wanted to make sure that this important driving force was as good as possible. The best alternative, therefore, is to take the sea-level information at the northern boundary of our model area as it is predicted by the operational model. This has the following advantages: (1) the signal is consistent with the spatial and temporal evolution of the large-scale circulation (tides plus wind), and (2) it is not corrupted by the noise due to the coarse resolution of the operational model south of the barrier islands. The sea-level records of tide-gauge stations on the barrier islands (most of them are located to the south of the islands) could be used for validation of our model results or, in a further study, for assimilation into the model.

We used the following procedure. The sea-level data from the operational BSH model (one value every 15 min) were interpolated in space and time onto the grid points along the northern boundary of our regional model (Fig. 4). For the meridional open boundaries in the west and east we simply took the value of the sea level from the respective point on the northern boundary because of the noisy fields in the BSH simulations close to the coast (see Fig. 5). This simple treatment possibly introduces some inaccuracies in the forcing due to small errors in phase and amplitude. However, the delay in tidal oscillations along the meridional open boundaries, with respect to the phase at the same longitude in the upper left (right) corner of the model grid, is relatively small. This is explained by the fact that the oscillations in the larger area to the east and west of the model area are strongly coupled to the oscillations in the open sea through the deep channels of the Jade and the wide inlet between the islands of Borkum and Juist (see Figs. 1 and 4). Even though the above arguments seem to be consistent, we admit that the simulations in the tidal basins adjacent to the eastern and western boundaries could be affected by the inaccuracies in boundary conditions. However, the watersheds separating the tidal basins tend to reduce the exchange between them, as well as the propagation of nonphysical signals. In Section 8 we will show that the major forcing in the tidal basins originates from the inlets, where the local dynamics are strongly coupled with the dynamics of the open sea. In this case, small errors introduced at the meridional open boundaries would not greatly affect the solution in the central tidal basins (south of the islands Norderney to Wangerooge), the latter being of major interest in this study.

4.2.2 Analysis of boundary condition data

For our regional model simulations we used BSH sea-level data for the period between October 10 to 18, 2000. This period includes one neap tide (from October 10 to 12) and one spring tide (from October 16 to 18). The temporal and spatial characteristics of the sea-level signal are shown in Fig. 7a,b for the spring tide and Fig. 7c,d for the neap tide. The time–space diagrams give the sea-level anomaly $\Delta\zeta(x, y = \mathrm{NB}, t)$ at the northern boundary ($y = \mathrm{NB}$), where we have subtracted the instantaneous mean value for the northern boundary (the black curves in Fig. 7b and d, see also Eq. 26). The slope of the sea-level changes substantially in the east–west direction over a tidal cycle, thus causing the wide excursions of the Lagrangian particles illustrated in Fig. 6.

During spring tide, the tidal range is ~ 60 cm higher at the eastern boundary than at the western one. During neap tide, this difference drops to ~ 40 cm and the patterns in Fig. 7c are smoother than those in Fig. 7a. In summary, the model forcing is characterized by three major variabilities of the sea surface: (1) it undergoes vertical oscillations which appear almost instantaneously over the whole domain because the scales of the domain are much smaller than the perimeter of the amphidromy in the North Sea, (2) it undergoes oscillations in an east–west direction because the region is dominated by the slope of the sea surface during the different phases of the tides, and (3) the oscillations are subject to an east–west asymmetry, i.e. the tidal range tends to increase to the east.

The tidal signal associated with the amphidromy travels through our model area in ~ 50 min. Thus, with

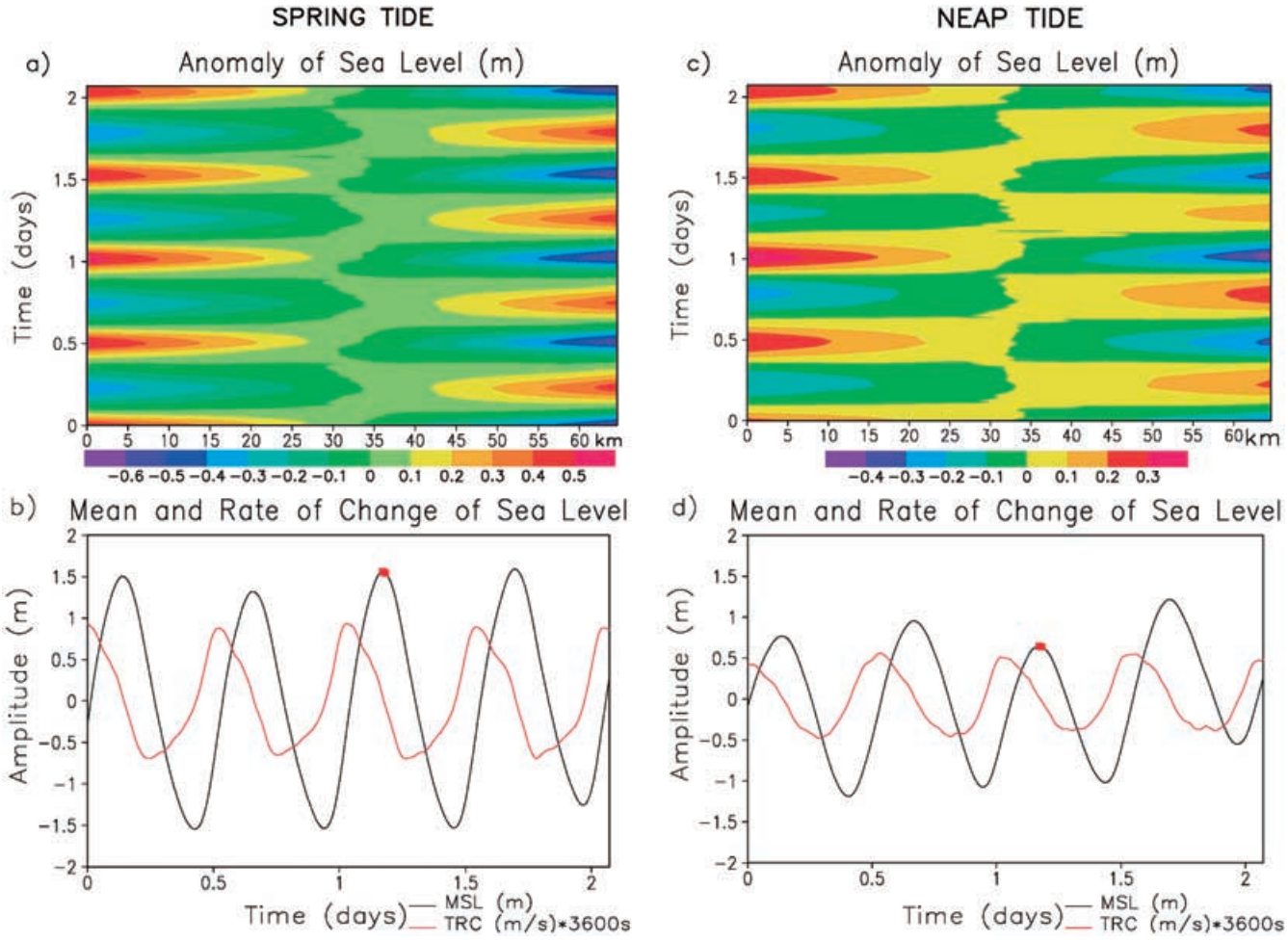

Fig. 7a–d Variability of sea-surface elevation at the open boundary of the model during spring (16–18 October, 2000, **a** and **c**) and neap (10–12 October 2000, **b** and **d**) tide periods. **a** and **c** are time-space diagrams of the sea-level anomaly, **b** and **d** are the mean signals for the whole boundary. The *red squares on the graphs* mark the time when high water occurs. We refer to these time markers in Sect. 5.1 when specifying the timing conventions used in the analysis of the simulated horizontal patterns. *MSL* and *TRC* stand for mean sea level and time rate of change, respectively (see the legends)

15-min intervals between the records provided by the BSH operational model, this process is relatively well resolved. However, for smaller model areas along the coast of the North Sea, the downscaling has to account for this resolution problem in the forcing data.

The tidal signal coming in from the open ocean undergoes large distortions in the shallow coastal regions, which includes relative changes in the amplitudes of the tidal constituents as well as asymmetry in phases. Given the fact that our northern model boundary is located over relatively shallow depths (at $\sim$ 15–20 m), we can expect that the forcing signal has already undergone some transformation compared to the composition of the tidal signal in the open part of the North Sea.

To describe the asymmetry of the tidal signal, we analyzed the time rate of change of sea level $\partial\zeta/\partial t$ during ebb and flood periods, which illustrates the transformation of the tidal signal associated with nonlinear interactions between oscillations with different periods, the relative increase of the role of friction in the shallow coastal zone, as well as local morphological effects (Aubrey and Speer 1985; Friedrichs and Aubrey 1988). As seen in Fig. 7b and d, the duration of positive anomalies in sea level is almost equal to the duration of negative anomalies. However, the time rate of change of sea level, which is directly connected to the magnitude of the tidal currents (see Eq. 2), is larger under flood than under ebb conditions. This type of asymmetry, known as flood dominance, is more pronounced during spring tide, and the simulations done with the BSH operational model reveal this asymmetry, supporting earlier observations in this area (Antia 1993).

4.3 Validation data from pile stations

Water level in the Wadden Sea has been recorded since the beginning of the 19th century and an extended analysis on data availability from tide stations is given in the papers of Lassen (1989) and Lassen and Siefert (1991). Two problems arise when looking for data for model validation: (1) all available data are from coastal

stations, and perhaps the signals are not quite representative for the open parts of the tidal basins and (2) time series of currents are not available in the region. However, without validating the simulated currents a proper model validation can not be done.

The data collected by the GKSS Research Centre (see Sect. 5) presented the first opportunity to validate our simulations of sea level and currents in locations far from the coast. The pile station near the Accumer Ee tidal inlet (53°42, 657′ N and 7°28, 273′ E, see Fig. 4b) was erected on May 24th, 2000, and was active until November 24th. It was equipped with the following sensors: water velocity in north and east directions (ADCP), optical transmission, water temperature, gauge level, water pressure, electrical conductivity, wave height, wind speed in north and east direction, air temperature, air pressure, and irradiation. The data were sampled at 10-min intervals, except for the wave height, which was recorded every 0.5 s.

Below we will address the consistency between observations (GKSS data) and model forcing (BSH data). The quality of the forcing data has been discussed already, and the general agreement with published tidal characteristics has been identified in Section 4.2. However, there are no tidal observations in the open sea adjacent to our model area with which we could compare the data from the BSH model. One partial solution is to examine the consistency between model forcing and observations. To give a better idea about how well the two data types correlate, we compare them not only for the period of our model integration, but for the whole period from the 10th to 18th of October 2000, which includes our two periods of integration. The differences in amplitudes between the two data-sets are to be expected and are due to the distortions of the signal after passing through the inlets and into the shallow back-barrier area. The coherence between the oscillations in the open ocean (model forcing) and the observed response in the back-barrier basin of Langeoog (Fig. 8) is quite remarkable. Not only are the general phase characteristics of the tidal signal well reproduced by the BSH operational model, but also the changes in amplitudes between neap and spring tide periods. The oscillations in the basin of Langeoog reveal a short time lag with respect to the oscillations at the open boundaries. For most of the period displayed in Fig. 8, the time lag is stronger during the ebb phase, which gives clear evidence that the distortions of the tidal signal in the back-barrier area are more pronounced during the ebb period.

5 Intercomparisons between observations and simulations

5.1 Data series

In the following we analyze the consistency between simulations and observations of sea level and currents at the location of continuous measurements carried out in the tidal basin of Langeoog and the transports through the main channel (see Fig. 4b for locations). The agreements between simulations and observations are better for sea-level (Fig. 9a,b) than for surface velocities (Fig. 9c,d). The phases almost coincide for the sea-level signal under spring tide forcing, whereas the amplitudes are slightly underestimated by the model. During the neap period, the model successfully reproduces the shape of the tidal signal. This is an important result because it is not a simple consequence of model forcing, i.e. oscillations in the back-barrier area are not linearly coupled to the oscillations in the open ocean. This statement is justified from Fig. 8, demonstrating that the difference between the amplitudes at the open model boundary (the forcing data from the BSH operational model) and the response in the tidal basin of Langeoog (estimated from the measured data at the pile station) is large. This difference is an indication of the transformation of the tidal signal in our model area, and not a drawback of the data. Comparing the amplitudes and phases of the simulated and measured signals in the location of the pile station (Fig. 9b), we discover a much smaller difference than between BSH data in area NS and GKSS data in the tidal basin. This proves that the model physics "propagates" the forcing signal into the back-barrier zone in such a way that simulations and observations agree reasonably well. Obviously, the transformation of the tidal signal in the coastal zone is thus resolved by the model.

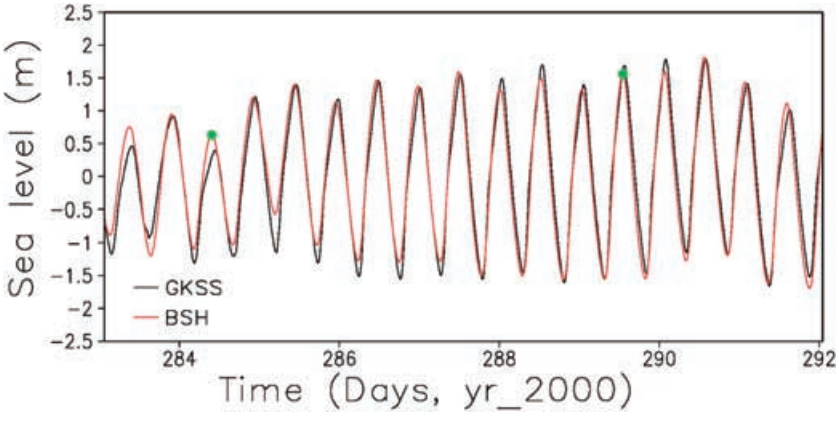

Fig. 8 Variability of sea level at the open model boundary (*BSH-red line*) and the observed variability (*GKSS-black line*) in the basin of the Island Langeoog during 10–18 October 2000

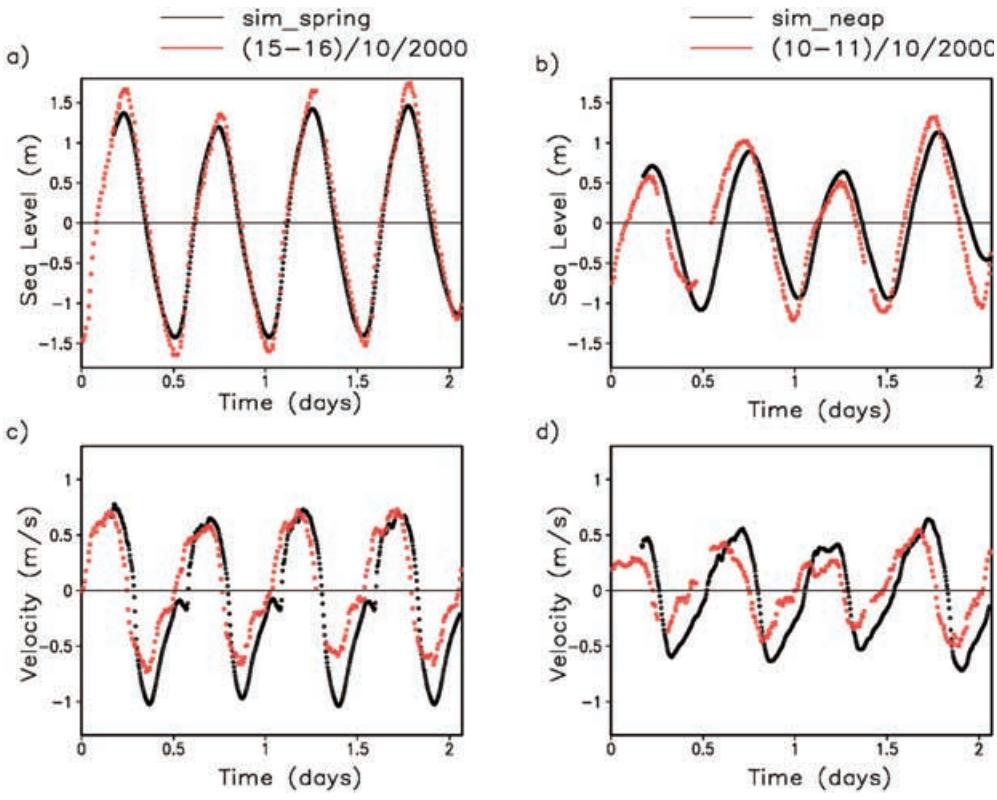

Fig. 9 Simulated and observed sea surface elevation (**a, b**) and currents (**c, d**) in the basin of Island Langeoog during spring (**a, c**) and neap (**b, d**) tide. Positive values correspond to transport toward tidal flats

The variability of surface currents is also well reproduced by the model (Fig. 9c,d). Of particular value is the agreement between the asymmetry of the oscillations in simulated and observed signals which are identified by the different slopes of the velocity curves. It is not only the major asymmetry of the transport curves which is reproduced by the model, but also some short duration features, the latter illustrating that: (1) the complex bathymetry of the model is well resolved, and (2) that filling and emptying of the back-barrier region in the model follows the natural regime. This proves that the model physics correctly reproduces the processes in the Wadden Sea.

Because the location of the measuring pile is in the main channel close to the inlet, the currents there to a large extent integrate the response of the Langeoog basin to external forcing. We conclude that the documented asymmetry in the curves provides a synthesized pisture of the transition of the physical system towards an ebb-dominated behavior (see further Sect. 7).

5.2 Cross-channel transects

The ADCP transects across the main channel in the Langeoog basin gave a unique opportunity to test the general dynamical characteristics of the local tidal basins associated with the bulk export-import of water, as well as its temporal variability. The transport integrated over a flood/ebb period defines the volume of water accumulated in, or exported from, the tidal basins. This fundamental parameter reveals whether the basin bathymetry is well resolved, this issue being of particular importance because the topography and coastline are subject to variable sedimentation, keeping in mind that the quality of bathymetric data is often questionable. The shape of the transport curves, on the other hand, is indicative of the physical response of the back-barrier area.

For the periods of integration we compute the transport through the Accumer Ee and compare it with the transports which are calculated from ADCP measurements. The data density (between 18 and 27 sections per tidal cycle during the different campaigns) is quite sufficient to resolve the variability in the flow. Unfortunately, the ADCP transects are measured at different times of the year, and we cannot directly compare the simulations carried out during two short periods of integration with transport data from transects. We therefore separate the observations into two categories: a spring and a neap situation. In Fig. 10 the measurements of three spring and neap tidal cycles are compared with corresponding simulations. Perfect agreement is not to be expected because the undersampling limits the comparability of the two data types. Nevertheless, it is clearly demonstrated that the shapes of the curves are very similar to the observed shapes, particularly under spring tide conditions. It should also be remembered that during the neap period analyzed in the paper, the tidal range was extremely low (Fig. 8) which, to a large extent, explains the differences between observation and simulation. Other reasons for the differences could

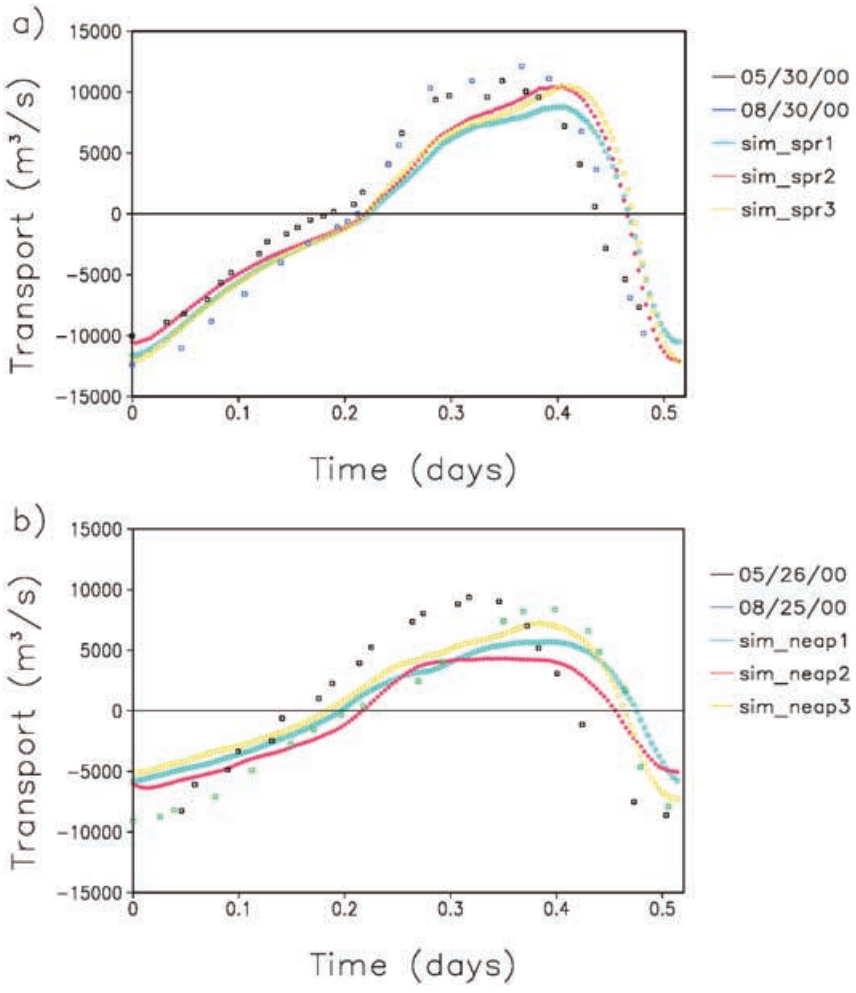

Fig. 10a, b Simulated and observed transports during spring (**a**) and neap (**b**) tides. Positive values correspond to transport toward tidal flats

originate from an insufficient grid resolution, as well as from topographic inaccuracies. In addition, it may be desirable to calibrate the bed roughness to the local conditions.

The general agreement between observations and simulations demonstrates that the model captures the basic dynamics of the model area. This result encouraged us to engage in a more extended analysis of simulated spatial patterns and temporal variabilities. This is a necessary step to understand the major dynamic controls in the region.

6 Horizontal patterns

6.1 Analysis of temporal evolution of circulation under neap and spring tides

A pronounced response to the forcing signal concerns not only the temporal variability, but also the horizontal patterns in the East Frisian Wadden Sea. Unfortunately, observational data are very sparse and it is thus difficult to gain a consistent understanding of spatial patterns and their evolution. In this respect, the results of numerical simulations are an important complement to the observations. Because the most vigorous dynamics is simulated during the periods of falling and rising sea level, we will illustrate the simulated horizontal patterns for the time of ebb and flood (Figs. 11–14). The timing can be seen in Fig. 7b,d, and the times EBB and FLOOD in Figs. 11–14 correspond to the 0.25 and 0.75 tidal period to the right of the time of high water, being represented by the red symbols in Fig. 7b,d. We recall here that the phase lag of the response with respect to the mean for the zonal open boundary signal is not constant throughout the model domain. On the other hand, the maximum in the time rate of change of sea level, which can be roughly taken as an indication of maximum current (Eq. 2), is slightly lagged against the ''zero'' water level, the latter coinciding approximately with the sampling-times (Fig. 7b,d). Obviously, the timing chosen to analyze the model results is largely subjective. To ensure that the discussion in the following sections reflects also the case when the timing is specified by the current maximum, we analyzed a large number of model outputs. Because no qualitative differences have been found, we have chosen an equidistant timing given by the external signal.

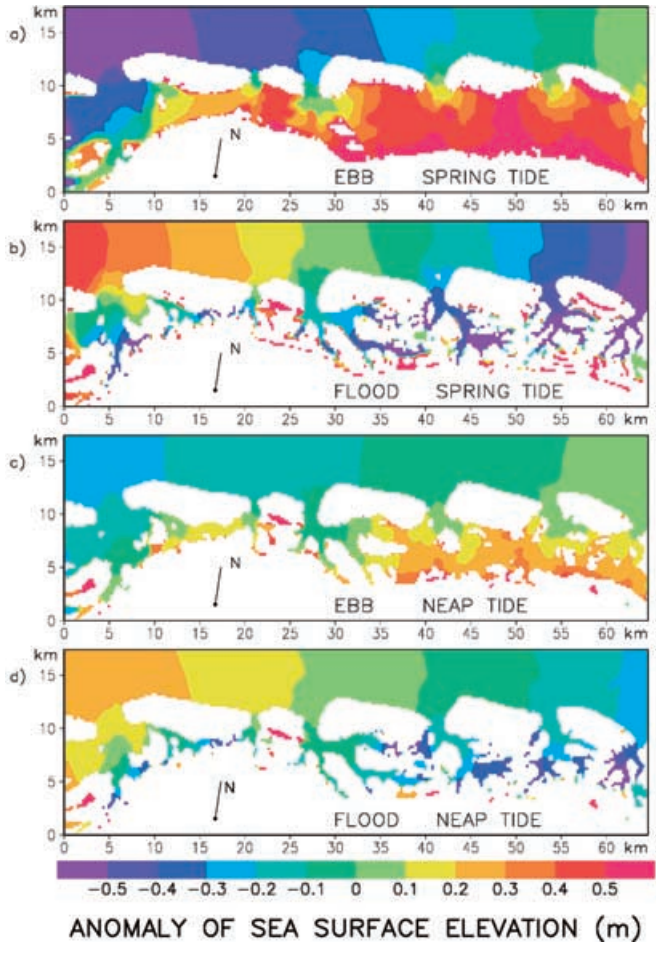

Fig. 11a–d Horizontal patterns of the sea-surface height anomaly (deviation from the current area mean value) during ebb (**a, c**) and flood (**b, d**) phases of spring (**a, b**) and neap (**c, d**) tidal cycle

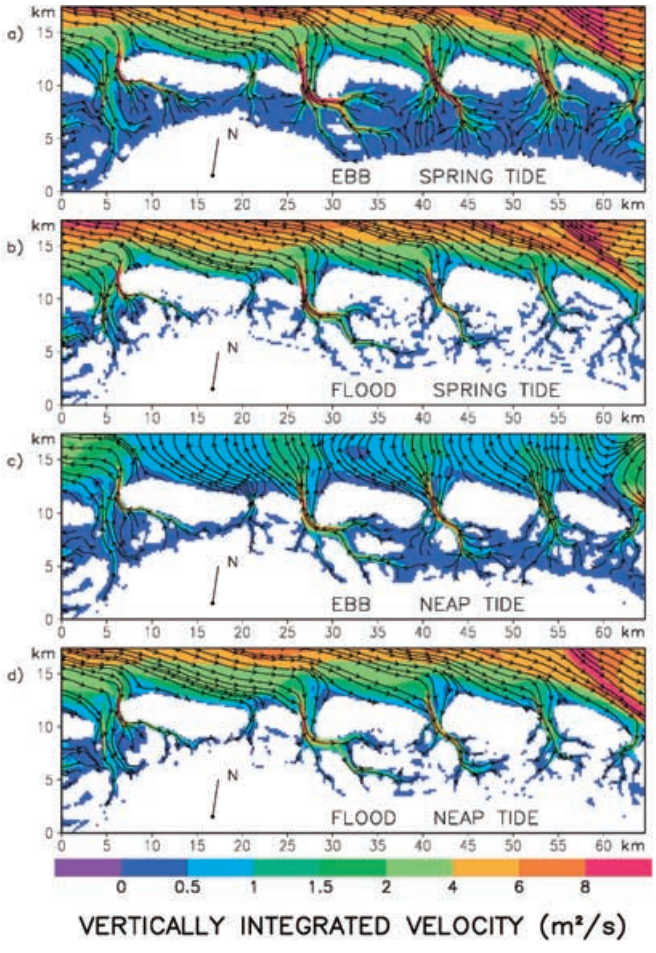

Fig. 12a–d Vertically integrated velocity during ebb (**a, c**) and flood (**b, d**) phases of spring (**a, b**) and neap (**c, d**) tidal cycle

6.1.1 Sea level

We start with an analysis of sea-surface elevation because it gives a clear picture of the dominating driving forces. In the shallow coastal regions these are mostly due to the horizontal pressure gradient. These gradients are shown in Fig. 12 as sea-level anomalies $\Delta\zeta(x, y, t)$, i.e. the difference between the local instantaneous value of ζ and the instantaneous area mean value of ζ (see Eq. 26). The gradient of the sea-level anomaly gives the horizontal pressure gradient, the temporal variability is represented by plots like the ones in (Fig. 9a,b).

The slope of the sea level north of the barrier islands is distinctly different during ebb and flood periods. During the ebb, we have a falling sea level and the slope is from east to west. During the flood, the slope north of the islands is from west to east. The circulation in the study area is thus dominated by westward transport during ebb and eastward transport during flood (see Fig. 12). This horizontal pattern of ζ is obviously an important ingredient of the driving force, considering that its maximum zonal difference of $\sim$ 1 m throughout the model area (including the open boundary) is comparable with the tidal range of $\sim$ 2–3 m.

The evolving pattern of the sea-level anomaly demonstrates how the model "extrapolates" the forcing from the open boundary into the model area, keeping in mind that at every moment the sea surface at the open boundary is a function of the zonal coordinate. This dependence actually introduces the information about the eastward propagating tidal wave and the variations of the tidal range along the open boundary into the model forcing. The zonally dependent signal easily penetrates southwards into the model area, as a result of which the isolines of the sea-level anomalies are almost meridionally oriented in the area between the model boundary and the barrier islands. Within the tidal basins, however, we observe a pronounced deviation from this pattern.

The major response characteristics in the tidal areas are associated with a delayed response of individual basins to the external forcing. In both phases of the tide (flood and ebb) the sea-level response in the tidal basins slows down relative to the signal north of the barrier islands.

The ebb situation during spring tide conditions illustrates the strong pressure gradient changes in the inlets. Over a distance of only 5 km, the sea level reaches differences of $\sim$ 40–50 cm. The situation is very different during the flood phase when the slope is smaller, but extends over longer distances along the tidal channels.

This indicates (for more detail see Sect. 6.1.2) that the currents are stronger during the ebb period, which could result in an ebb-dominated asymmetry in the tidal basins. The latter situation is not as pronounced during neap tide conditions. What is peculiar in the ebb pattern simulated under spring tide forcing, is that the high sea level in the tidal basins does not "see" the deep channels, but only the inlets (the gradients are large only in the vicinity of the inlets). During the flood phase (when the shallow flats are still dry) the signal of rising sea level propagates throughout the channels with a level difference of ~ 40 cm during the spring tide and ~ 20 cm during neap tide.

The comparison of the spring and neap tidal patterns clearly shows that it is not only the tidal range which causes the main difference between the two situations, but also the properties of the incoming tidal wave from the west. The steepness of the tidal wave is smaller during the ebb (cf. Fig. 11 a,c with Fig. 11 b,d, correspondingly), and this is one of the reasons why the circulation north of the barrier islands is less vigorous during the ebb period. The comparison of sea-level anomalies and velocity patterns reveals also that a geostrophic transport is unlikely in the Wadden Sea (during ebb, the currents in the inlet approximately follow the slope of the sea level). The major balance dominating the circulation in the Wadden Sea is that between pressure forces and friction, i.e. the influence of the Coriolis acceleration is relatively small in our model area (compared to the case of open ocean). Nevertheless, B.W. Flemming (personal communication) observed stronger flood currents along the western channel margins and stronger ebb currents in the center and eastern channel margins.

During both tidal phases (flood and ebb) the sea level in the tidal basins tends to adjust to the sea level outside. The perturbations thus propagate along the channels because they provide the major pathway for the signal in the tidal basins. The delay of the response in the channels depends on the relative position of the tidal inlet with respect to the wave front. That is why the situation in the eastern basins (e.g. the basin of the island Wangerooge) seems to be coherent with the oscillations in the open ocean, whereas south of the islands Juist and Norderney the along-channel difference of the sea level is much higher ($\sim$0.5 m), being particularly pronounced during the flood phases of both tides (Fig. 11b,d).

6.1.2 Currents

The simulated currents in the outer model area are consistent with the circulation simulated with the BSH operational model (cf. Fig. 12 a,b with Fig. 6). The general direction of the transport is to the west during the ebb phase, and to the east during the flood phase (remember that we use a slightly rotated coordinate system). The currents are less aligned to the isobaths during the neap-tide period, which results from the fact that during that period the alongshore slope of the sea-level is smaller. Correspondingly, the meridional component of the velocity is more pronounced in Fig. 12c than in Fig. 12a, and the speeds are smaller (not only in the tidal inlets, but also in the North Sea part of our model). It is obvious that while the transport through the inlets is mainly governed by the amplitude of the tidal oscillations (see Eqs. 1 to 2), the alongshore circulation, as well as the circulation in the intertidal areas, is governed by the spatial properties of the forcing signal. During the whole period of integration, the circulation under spring tide follows a clear Z-shaped pattern (approximately east–west in the NS area, north–south in the inlets, and again east–west in some of the tidal basins). The curvature of the profile decreases at neap tide mainly as a consequence of the changing rate between the tidal range (responsible for the strength of inlet outflow) and the alongshore sea-level gradient at the open boundaries, the latter accelerating the alongshore current.

6.1.3 The TKE and EDR

In the Wadden Sea the major physical balances are largely controlled by friction. The patterns of turbulent kinetic energy (TKE) and the eddy dissipation rate (EDR) in the deepest layer of the model shown in Figs. 13 and 14 give an impression of the dissipative properties of the model. It should be noted that so close to the bed, TKE and EDR are governed by the law of the wall with

$$k = \frac{(u_*^b)^2}{c_\mu^{1/2}}, \qquad \varepsilon = \frac{(u_*^b)^3}{\kappa(z' + z_0)} \quad , \tag{27}$$

with z' being the distance from the bed.

Both TKE and EDR show absolute maxima in the tidal inlets, which demonstrates that the frictional control occurs in the inlets. The major (and topographically similar) inlets of Harle, Otzum and Accum show a very similar behavior during the ebb, particularly in the dissipation. These patterns are characterized by a funnel-like widening in the region of the tidal deltas (north of the inlets), as well as in the back-barrier area during spring tide. The small patches of very low TKE and EDR levels in the back-barrier area (Figs. 13a and 14a) approximately coincide with the watersheds separating the individual basins (cf. Fig. 4).

The northern coasts of the barrier islands are characterized by weak levels of tide-generated turbulence (Fig. 13a,b), thereby promoting accumulation of suspended particles in these areas. The patterns of TKE

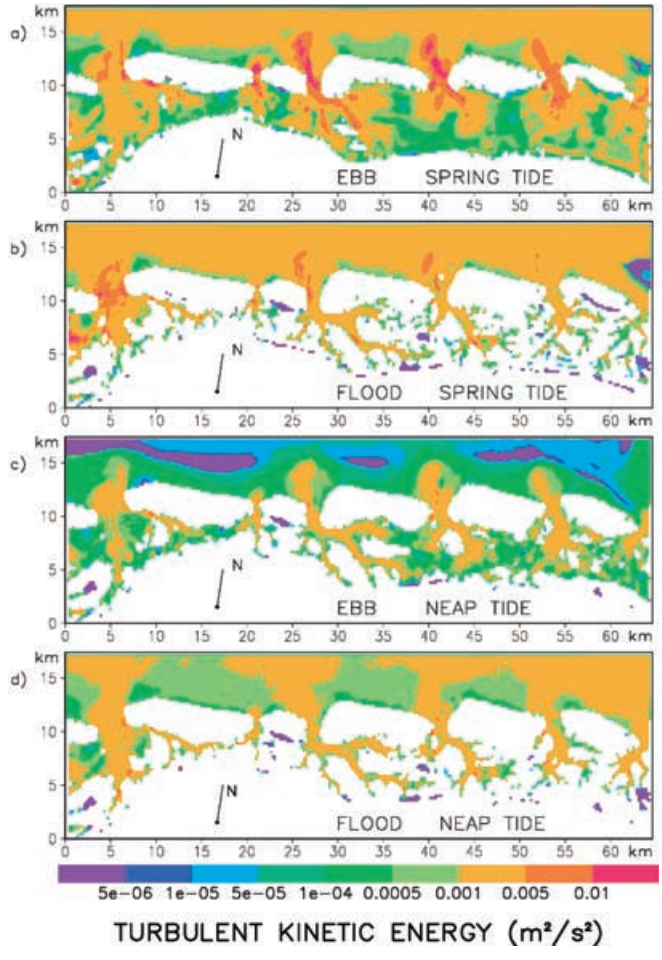

Fig. 13a–d Horizontal patterns of the bottom turbulent kinetic energy during ebb (**a, c**) and flood (**b, d**) phases of spring (**a, b**) and neap (**c, d**) tidal cycle

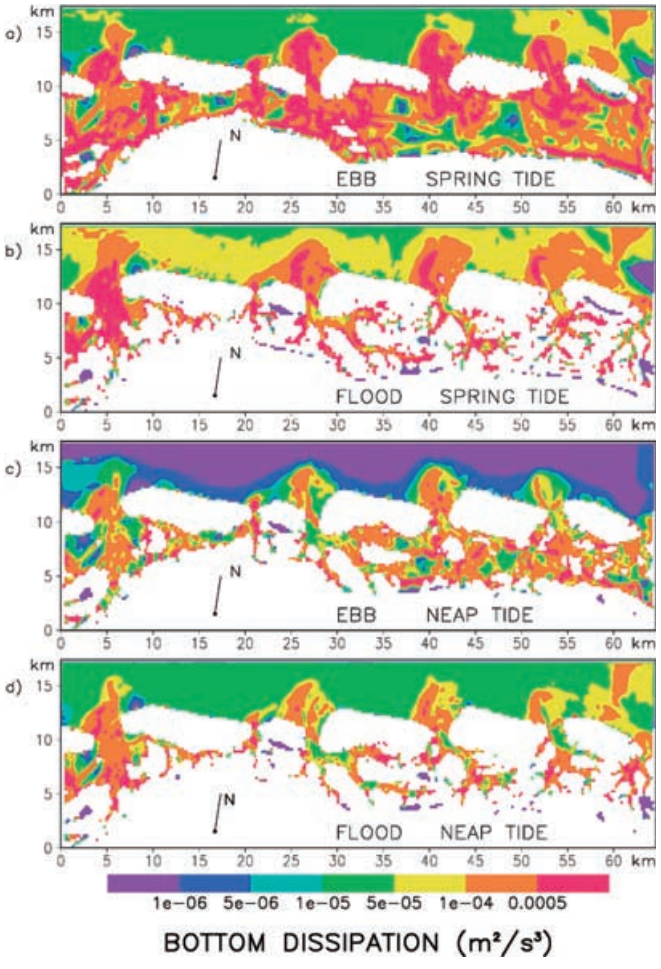

Fig. 14 As in Fig. 13, but for the dissipation rate

(Fig. 13) and in particular the patches with small values along the northern coasts of the islands and in the tidal basins (Fig. 13a), are therefore favorable for the accumulation of sediments, although wave action would in some cases contradict this effect. Most of the barrier islands display three areas of minimum TKE values. The first two are situated north of the barrier islands near the eastern and western tips. The third one is located along the southeastern shores, and is (in most cases) connected with the area of minimum TKE on the watersheds. We emphasize that this pattern reflects the case of no-wind waves. Further studies are obviously needed to account for this effect.

The patterns displayed in Figs. 13 and 14 are characteristic of the extreme conditions, corresponding approximately to times when the transport through the inlets reaches a maximum. During the remaining part of the tidal cycle (the times of high and low water), the TKE and EDR have much smaller magnitudes, particularly north of the barrier islands (the horizontal patterns are not shown here, but the meridional dependence of TKE during different tidal phases is addressed in Sect. 7). The complex temporal and spatial patterns thus contribute to the formation of complex friction properties in the model area, which have a number of practical consequences, in particular the physical control on the morphodynamics.

The erosion capabilities in our model area can be roughly estimated by taking the critical bed shear stress as 0.4 N m^{-2} which is sufficiently high to trigger erosion of bottom sediment (Santamarina Cueno and Flemming 2000). This value corresponds to a friction velocity of $\sim 2\,cm\ s^{-1}$, and is always reached in the tidal channels (especially during spring tide), as well as in most areas of the North Sea part of our model area (Antia 1993). In fact, the inlets erosion ceases only for very short time periods only (see Sect. 7).

At the end of this section we wish to reiterate one particular characteristic of GETM, i.e. its ability to reproduce the periodic drying and flooding of the tidal flats. This is illustrated in Figs. 11–14 by the differences in land–sea masks. In the GETM these masks are not prescribed, but are a product of simulations. It is noteworthy that the water coverage during the two ebb and flood situations differs considerably. The main difference is evident from the two ebb situations. Obviously, it takes more time to export the larger volume of water

stored on the tidal flats during spring tide (cf. Fig. 12a and b) the rate of drying being thus retarded in this case. This result demonstrates the sensitivity of the position of the moving model boundary, particularly in the extremely flat model area, to small differences in tidal elevations (see also Fig. 5).

6.2 Residual circulation

The residual currents reveal similar patterns during spring and neap periods (Fig. 15). Areas of large residual transport are in the tidal channels and ebb deltas, as well as north of the inlets. We recall that one important mechanism generating residual currents is the interaction between currents and topography, and this has been addressed in a number of studies (e.g. Huthnance 1973) documenting and explaining the interaction between circulation and sand banks.

Our simulations reveal minimum residual velocities at the northern model boundary and on the tidal flats between the tidal basins. The plausibility of the simulations is supported by the velocity minimum in the output of the BSH model (Fig. 6), where several patches with velocity minima are reproduced in the same areas.

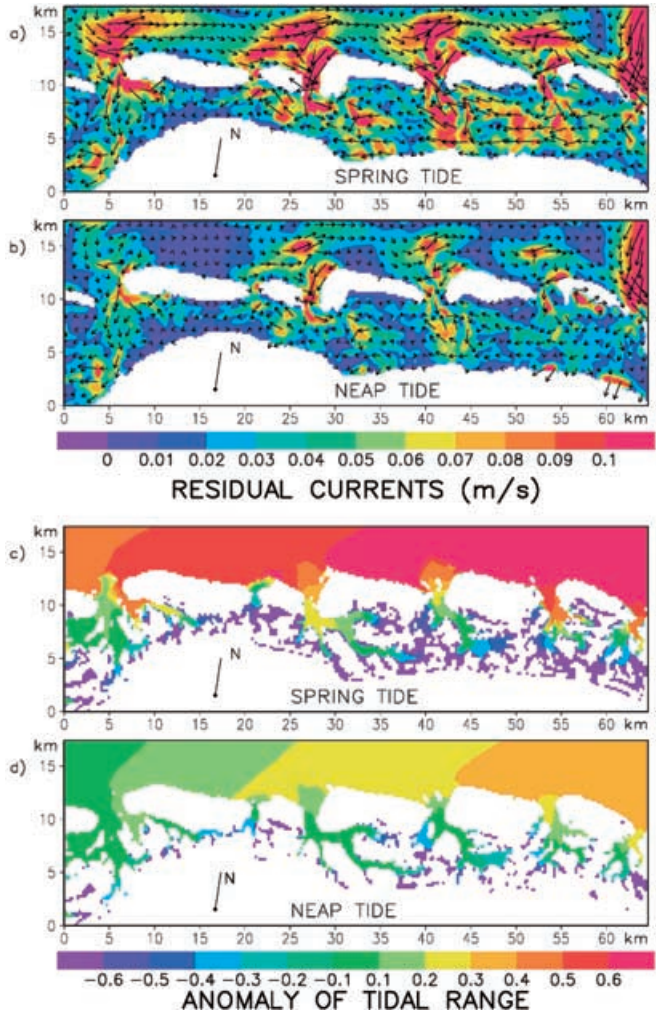

Fig. 15 Residual currents during spring (**a**) and neap (**b**) tide. Anomaly of tidal range during spring (**c**) and neap (**d**) tide

The predominant eastward transport reaches maximum values north of the inlets, but it almost vanishes shortly after the current starts to flow along the coast. This process could contribute to the export of sediments from the western part of the islands and its deposition in the eastern part.

There is an overall compensation of the eastward transport along the north coasts of the islands by a transport in the opposite direction over the tidal flats. During neap tide (Fig. 15b) the magnitudes of alongshore transports are much smaller. This supports the notion that the formation of residual currents depends on nonlinear effects which are amplified under spring tide conditions (in our simulations the range of the sea-level oscillations during neap tide is $\sim 60\%$ of the range during spring tide). Obviously, the strength of forcing is not only a function of the tidal range r, but also of the ratio between r and the depth of tidal basins H_m. In the case of Spiekeroog, and for the tidal signals used in our simulations, this ratio is ~ 1.17 under spring tide conditions and ~ 0.87 under neap tide conditions (see the fifth lines in Tables 1 and 2).

The nonlinearity in some coastal systems could result in larger amplitudes of water-level oscillations in the tidal channels as compared to the areas outside. Whether this is also the case in our simulations can be seen in Fig. 15c,d, where the anomaly of the tidal range is shown for the period of integration. Only in the easternmost inlets is the tidal range comparable to the range outside the channels. This again demonstrates that the most vigorous dynamics are observed in the inlets. In the rest of the model area, and in particular during neap tide periods, the tidal range decreases with decreasing distance from the inlets. Our sensitivity experiments with stronger forcing or modified topography have demonstrated that tidal ranges can, in principle, reach maxima in the inlets under certain conditions.

The above results should be regarded as preliminary estimates about the residual circulation and patterns of tidal ranges. We admit that they might depend on model numerics, and in particular on the advection scheme. We recall that the first-order upstream scheme used here is monotonous but quite diffusive. It is shown by Burchard and Bolding (2002) that the residual currents are significantly stronger when higher-order advection schemes are used but their direction is basically unchanged by the schemes. More important is to note that the averaging in time can also lead to some differences, depending on the length of time considered. Therefore, the residual circulation in the East Frisian Wadden Sea will still be subject to further investigations using models with higher-order advection schemes, better horizontal resolution, and more complete forcing. However, the anal-

ysis of longer-time simulations (not discussed in this paper) and larger amount of residual outputs led us to the conclusion that Eulerian displacements (reaching more than ~ 5 km during one tidal cycle) are comparable with the tidal excursions (see Fig. 6). Such systems can develop strong mixing. It has been demonstrated by Ridderinkhof and Zimmerman (1990b) that dispersion is enhanced by spatial velocity variations if the latter have length scales shorter than those of the tidal excursions. Dynamical systems of this type could produce chaotic mixing.

7 Temporal and spatial asymmetries

7.1 Tidal asymmetry

The inlets of the East Frisian Wadden Sea are a pronounced feature in the local bathymetry, created and sustained through a subtle balance between the acting physical processes which shape the exchange between tidal flats and the open ocean. Numerous observations (e.g. Santamarina Cueno and Flemming 2000) demonstrated that maximum velocities exceed 1 ms^{-1}, and our simulations support these earlier results. The analysis of simulated data shows that there is an overall similarity between the dynamics in the individual inlets, particularly in the larger ones (from Harle to Accumer Ee). Some differences are associated with the delay of the tidal cycle along the shore. Thus, the transport maxima in the Harle inlet occurs ~ 1 h later than in the Norderney inlet.

In the following, the evolution of the tidal dynamics using the tidal inlet between the islands Langeoog and Spiekeroog (i.e. the Otzumer Balje) is taken as an example. The time-versus-depth plots of the simulated transport and turbulence characteristics shown in Fig. 16 are coherent with the observations in tidal basins. Two velocity maxima are simulated every tidal period.

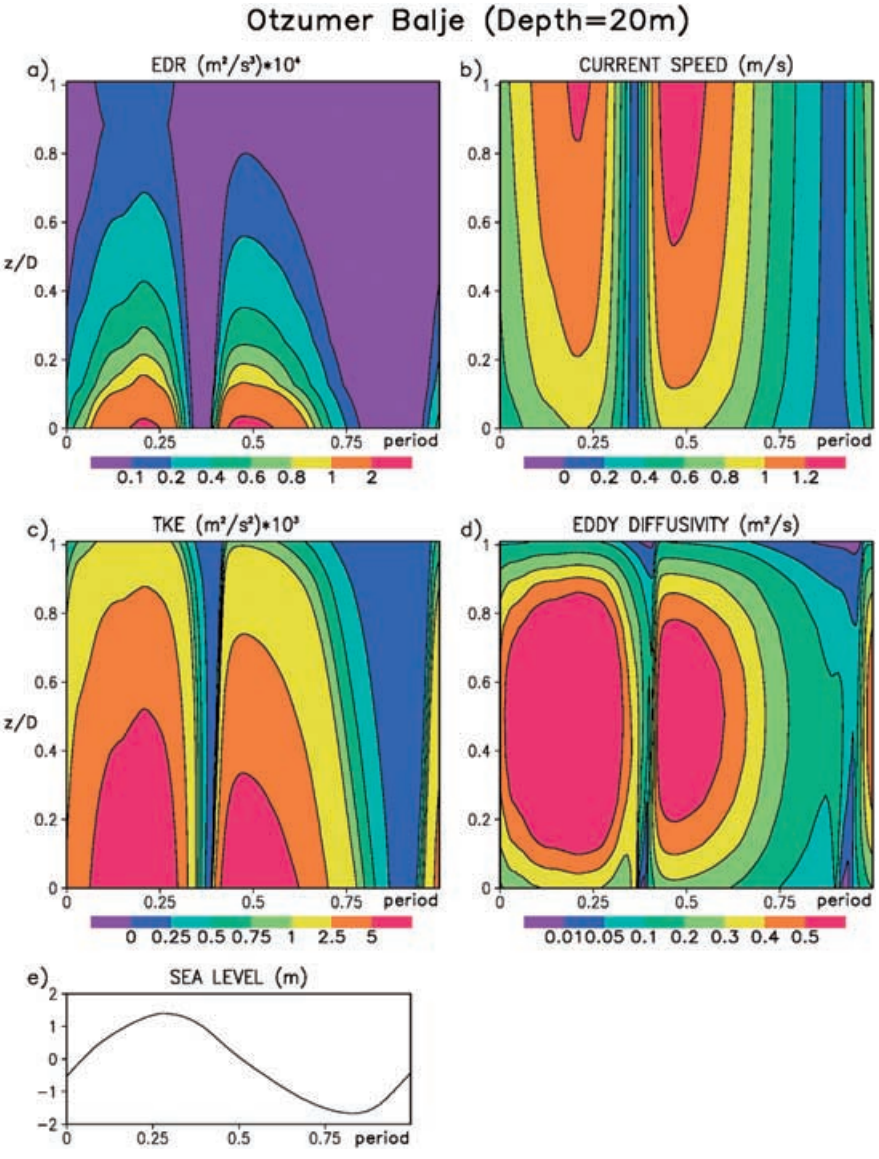

Fig. 16a–e Time-versus-depth plots during spring tide in the Otzum Inlet (the location noted by the *diamond* in Fig. 4d). **a** The dissipation, **b** the magnitude of velocity, **c** the turbulent kinetic energy, and **d** the coefficient of turbulent exchange. The *bottom plot* **e** gives the sea level at the open boundary at the same latitude and for the same period as a **a–d**

The first maximum corresponds to the flood and the second to the ebb (see also the bottom panel of Fig. 16). Most of the time the entire water column shows relatively strong vertical gradients in velocity and therefore a high level of turbulence. Only during slack water (duration of ~ 1 h) do the vertical velocity gradients vanish, and the level of turbulence diminishes.

The time rate of change of all values shown in Fig. 16 is larger in the period of transition from flood to ebb. The TKE is quite high in almost the whole water column, which could contribute to maintaining favorable conditions for erosion over most of the tidal period. The light blue color approximately corresponds to the condition when the friction velocity begins to exceed $0.02\ \mathrm{ms}^{-1}$. Sedimentation will prevail in the inlets during the slack water periods, and in particular during the relatively longer low-water phase ($\sim$ 3 h) when the conditions are much less energetic.

Figure 16 clearly demonstrates the asymmetry of the simulated tidal signals. This important characteristic of tidal basins dynamics is sometimes understood to merely reflect some sort of tidal dominance, i.e. when the flood current is strong and persists for a shorter time we have flood dominance, whereas the opposite situation is called ebb dominance. In our simulations the maximum velocity is only slightly larger during ebb. However, more important is to note that the asymmetry of the signal is much better seen in the difference between time periods during which the maximum flood and ebb are established. Our simulations demonstrate that a longer time is needed for the transition from maximum outflow to maximum inflow, i.e. it takes longer to decelerate the ebb flow and to accelerate the flood flow than it takes to decelerate the flood flow and accelerate the ebb flow, respectively.

This indicates that the physical system in the tidal basins is very strongly affected by friction which "opposes" the establishment of a maximum flood velocity, but does not substantially slow down the process of reaching a maximum ebb velocity. We recall here that the maximum ebb velocity is simulated approximately when the rate of sea-level fall reaches its maximum at the open boundary. However, the maximum flood velocity is delayed by ~ 2 h with respect to the maximum rate of sea-level rise at the open boundary.

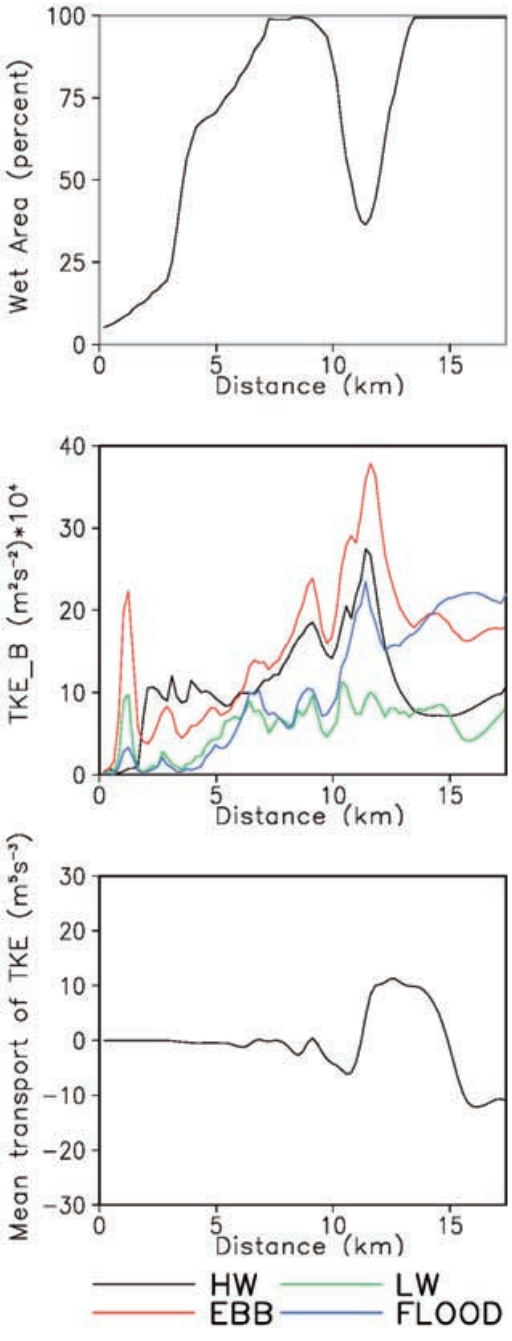

Fig. 17a–c Time and zonally averaged characteristics of turbulence. **a** Water coverage. **b** TKE at the bottom. **c** The product between meridional transport and TKE

7.2 Asymmetrical transport patterns

A conclusion from the analysis above is that ebb dominance is associated with a more efficient export of waters taking less time than needed to refill the basins. This does not necessarily imply, however, a continuous export of particulate matter. To understand the cross-shore transport capabilities in the model, we analyzed the zonally averaged model data. The water coverage of the model area as a function of distance from the coast is shown in Fig. 17a. The local minimum at ~ 12 km from the coast is due to the fact that the barrier islands are located at this position, thus reducing the wet area. At the same location, i.e. where the deepest sections of the inlets occur, we observe a TKE maximum. Figure 17b demonstrates that turbulence reaches its maximum during the ebb.

We can speculate, then, that the higher level of turbulence would result in higher erosion, and correspondingly suspended matter concentration. Supposing a positive correlation between bed shear stress (or TKE, see Eq. 27) and the concentration of suspended matter,

the correlation between transport and TKE would give an indication of the direction of suspended matter transport. The results in Fig. 17c indicate that an asymmetric transport is established north and south of the island chain: i.e. towards the open sea north of the islands and toward the coast in the south. The turbulence is obviously generated in the inlets, promotes erosion, and the currents tend to export the suspended matter from there.

Another peculiarity of the transport patterns is associated with the intense transport along the northern model boundary during ebb and flood (Fig. 12). This is reflected in Fig. 17b by the large level of bottom turbulence at these times. However, contrary to the case of the tidal basins, the bottom turbulence reaches higher values during the flood (we recall that in the area NS the flood signal is dominant). This specific correlation explains the negative (southward) direction of the transport south of the open boundary.

The product between transport and turbulence is intimately related to the sedimentation/erosion conditions and morphodynamics, and we can expect that the correlation between the transport and turbulence in the model, along with the asymmetry discussed above, have a net effect on the process of sediment sorting and sediment export/import. This effect in the model, when coupled with a dedicated sediment module, will probably contribute to shoreward transport of sediments in the tidal basins. This is actually the case observed in the back-barrier area (Nyandwi and Flemming 1995), and the model data reveal that the correlation between velocity and TKE might contribute to a net (shoreward) transport.

8 The temporal variability of area-averaged mass balances

In this section the overall balances are presented on the basis of area mean values, the focus being on the basin behind the island of Spiekeroog, which is representative for the processes in the basins behind Langeoog and Wangerooge. In Fig. 18a,b the time rate of volume change, the transport through the Otzum inlet, and the exchange with the neighboring tidal basins (normal to the lines separating the individual basins) is shown. By dividing the values plotted on the curves in Fig. 18a,b by the basin area (cf. Tables 1 and 2), the time rate of change of the mean sea-surface elevation is obtained.

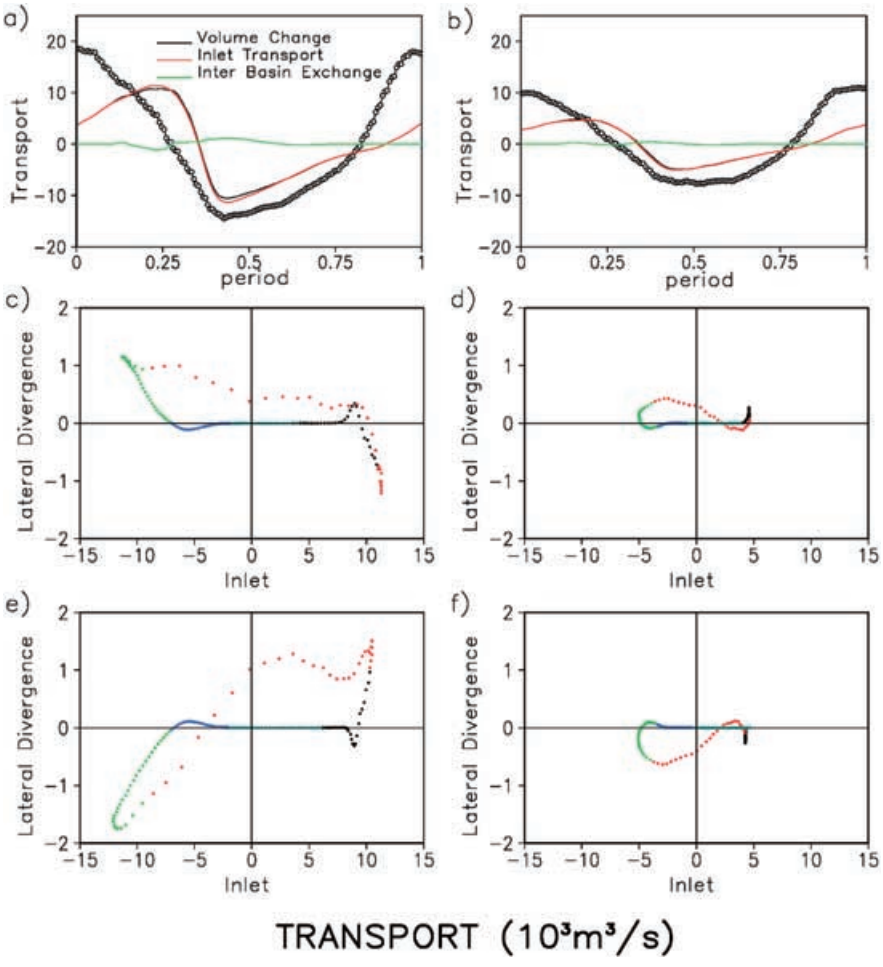

Fig. 18a–f Mass balances. The *left column* (**a, c, e**) is for the spring tide, the *right one* (**b, d, f**) is for the neap tide. **a** The change of volume in the Spiekeroog basin (*black line*), the transport in the Otzum Inlet (*red line*, the positive values indicate inflowing into tidal flats water), and the net change of volume due to interbasin exchange (*green line*). The *symbol(circle)-line is* the normalized change of volume in the outer area. **c** Scatter plot indicating the correlation between the transport in the Otzum Inlet and the net change of volume due to interbasin exchange. **e** The same as **c**, but for the Accum Inlet. The *sequence of colors* (black, red, green) gives the direction of rotation

In order to facilitate the understanding of the relationship between forcing and response, the normalized time rate of volume change in area NS is also shown (the symbol line in Fig. 18a,b). This area provides the forcing for all tidal basins, and the symbol lines in the graphs illustrate its temporal variability. The time rate of volume change in area NS has been normalized because the values are much larger than the corresponding ones in the Spiekeroog area (mainly due to the much larger NS area). The normalization is done by multiplying the simulations with the factor A_m^{Sp}/A_m^{NS}, where A_m^{Sp} and A_m^{NS} are the areas of Spiekeroog and the North Sea calculated for mean m sea level. Alternatively, the simulated data could be presented on a separate graph, or on the same one, but with two different scalings of the y axis. However, the normalized curve has the advantage of giving the time rate of change in area NS in units comparable to those of the Spiekeroog basin.

Suppose that the sea-level variability in the entire area NS is described by the symbol lines in Fig. 18a,b, and the sea level in the individual tidal basins follows the same course. We will call the response in this idealistic case (of horizontal sea level) no dynamical response. The difference between the forcing (symbol lines) and the simulations (the black lines) is thus indicative of the role of the dynamics. Under weak forcing (neap tide), the back-barrier system evolves more synchronously with the outer basin (the response signal in Fig. 18b shows less deviation from the forcing than in the spring tide case, Fig. 18a). Under strong forcing (spring tide), the nonlinear and frictional effects become more dominant, and the transition from flood to ebb is very sharp. Our model thus supports the widely held notion that in shelf areas and embayments with large intertidal flats the forcing signal is distorted in such a way as to establish ebb dominance.

The simulations clearly demonstrate that the transport between the basins (in the absence of wind) is much smaller than the transport through the inlets. This is the reason why the volume changes closely follow the inlet transport (see Fig. 18a,b). This result suggests that most of the difference between the sea-level variability in our model subareas is controlled by the inlets.

The level of response is weaker than the level of forcing, indicating that, on the average, the nonlinearities in the response are damped by friction. The oscillations are delayed with respect to the external forcing, particularly during the flood. This, again, demonstrates the asymmetry of the response, shaped by the large intertidal flat areas, resulting in the formation of ebb dominance.

The forcing signal reveals exactly the opposite tendency. The time rate of volume change in the NS area, which is approximately equal to the inflow at the open boundaries (considering that the transports through the inlets are small compared to the transports across the large open boundaries), shows that flood velocities are higher, i.e. the signal in the NS area is flood-dominated. The difference between the processes in the tidal basins and the NS area are explained by the data listed in Tables 1 and 2. The shallow depth in the NS area is favorable for establishing flood dominance (see also Sect. 3.2). Observational support of the above results is given by Antia (1993).

Every basin shows individual correlations between the inlet transport and net transport, which is due to the throughflows from the neighboring basins. This "lateral divergence" (y axis in Fig. 18c–f) is about 1 order of magnitude smaller than the transport through the inlets. This correlation does not only change dramatically between spring and neap tides (cf. Fig. 18c and f), but undergoes changes in the neighboring tidal periods, revealing the large sensitivity of interbasin exchange to small differences in the model forcing. Even larger are the differences between the correlation patterns simulated in the different basins (compare the situation in the basin of Spiekeroog, Fig. 18c, with the one south of Langeoog, Fig. 18e). Obviously, the interconnected individual regions of the East Frisian Wadden Sea function quite differently. It seems that the overall behavior of the Spiekeroog basin, for instance, is such that, under the forcing conditions considered here, it exports water to the neighboring basins during the flood and imports water during the ebb tide.

9 Conclusions

The application of 3-D numerical models is much more difficult in comparison to simple analytic models or models with a reduced number of dimensions. The results of simulations are physically not always quite clear because the numerous forcing parameters and multiple-response mechanisms are difficult to be separated. However, this is also the situation in the real basins, and increasing the realism of processes is the only way to perform comprehensive studies on the physical balances controlling the circulation in the East Frisian Wadden Sea, and in particular on the relationships between spatial and temporal patterns. This issue has thus far not been addressed in the physical oceanography of this region. Furthermore, studies generalizing the dominating response characteristics as dependent on the external forcing, local conditions, and governing dynamics are still lacking. The present paper is a contribution in that direction, being based on new and reliable physical information derived from numerical simulations. The reliability of this information is demonstrated by the verifications against observations.

There are several important prerequisites for our study, namely the availability of an adequate numerical model, adequate forcing data, and last but not least, observational data for the verification of the simulations. The most important model development ensuring the realism with respect to the regional conditions is the detailed description of the physical processes in the boundary layers and the vertical mixing parameterizations based on the k–ε turbulence model. This is of the

utmost importance because the barotropic Froude numbers are large in our model area. This gives theoretical justification to the assumption that friction should play an important role in the process of tidal distortion. The entire model area is very shallow and, due to this, as well as to the vigorous forcing, the entire water column is turbulent during most of the tidal period. As demonstrated by our simulations, friction at the seabed tends to slow down the tidal signal in shallow water which leads to the establishment of flood dominance in the NS area. Another consequence of the shallow bottom is the strong ageostrophic transport (during ebb the currents in the inlet follow approximately the slope of sea level). This proves that the major balance dominating the circulation in the Wadden Sea is between pressure forces and friction, i.e. the influence of the Coriolis acceleration is relatively small, but not negligible.

The second important model "ingredient" is the implementation of drying and flooding of intertidal flats. This is extremely important because the depth in the tidal basins is comparable to the tidal range. In this case, the permanent water storage in these basins is smaller than the tidal prism; the export and import of waters through the inlets have different characteristic times at low and high water. This leads to the establishment of an ebb-dominated response. Such response characteristics are found in many other similar basins, and the deep and long ebb channels in the area of the East Frisian Wadden Sea are the morphological expression of this situation. Our simulations reproduce this fundamental transformation of the signals, and support the observations. The asymmetry of the signals is demonstrated in the difference between the duration of the periods when maximum flood and ebb are established: it takes a longer time for the transition from maximum outflow to maximum inflow, i.e. it takes longer to decelerate the ebb flow and to accelerate the flood flow. The asymmetry is also a function of the tidal range. During neap tide the back-barrier system evolves more synchronously with the NS area than in the spring tide case. Under strong forcing (spring tide), the nonlinear and frictional effects become dominant and the transition from flood to ebb situation is very sharp.

The model setup is based on up-to-date forcing data provided by the operational model of the German Federal Maritime and Hydrographic Agency. The critical analysis of these data gives us the confidence that they provide correct forcing along the zonal open boundary of our model. The intercomparison with the observations in the back-barrier basin of the Island Langeoog demonstrated that phase characteristics of the tidal signal are well reproduced by the operational model. The lack of sufficient resolution in the nearshore region motivated us to develop our downscaling approach in order to increase the realism of the simulations in this area.

The forcing data resolve the tidal wave associated with the well-known amphidromy at $\sim 55.5°$N, $\sim 5.5°$E very well. We demonstrated that it is not only the vertical motion at the open boundary which is important for the circulation in the region. The oscillations provide sea-level differences in west–east direction of ~ 1 m which triggers tidal excursions in the NS area, which are comparable with the horizontal scale of our regional model. During the ebb, the slope of the sea level in the NS area is from east to west. During the flood, the slope north of the islands is from west to east. The circulation is therefore dominated by westward transport during ebb and eastward transport during flood. This regularity does not hold in the inlets, where the north–south component of the current is more pronounced, thus contributing to the formation of a clear Z-shaped pattern of streamlines. The curvature of the streamlines decreases under neap tide conditions mainly as a consequence of changing the rate between the tidal range (responsible for the strength of inlet outflow, which creates a northward current) and the alongshore sea-level gradient at the open boundaries, the latter accelerating the alongshore current.

Another crucial forcing mechanism is the steepness of the tidal wave along the open boundary of the model. This steepness is smaller during the ebb, and this is one of the reasons why the circulation north of the barrier islands is less vigorous during the ebb period.

Our simulations give a reliable tool for the estimation of turbulence in the water column and its temporal and spatial patterns. The latter controls not only the dissipation properties of the model, but also the transport of suspended matter (in the real ocean). The TKE and EDR show absolute maxima in the tidal inlets, which demonstrates that the frictional control is located there. The second area of active turbulence is along the northern boundary. Here it is caused by the large zonal transport and relatively shallow depths.

A large number of studies on the geomorphology of tidal basins address the relationship between the volume of the tidal prism and the cross-section of inlets. The correlation between these fundamental morphological parameters, which has been found in a wide range of natural settings (see the review of Bruun 1978), reveals that the erosion (controlling the cross-section of the inlets) and sedimentation (controlling the accumulation of sediment on the flats) are linked through the physical balances. By providing the feedback mechanism, the physical processes tend to adjust the geometry of the inlet to the volume of the flooded area. This is the most important process maintaining the tidal basins in a state of quasi-equilibrium.

Numerical simulations can provide the quantitative physical background needed to understand morphodynamics by giving at least first-order estimates about the transport of suspended matter. As a first step in this direction, the tendency for transporting turbulence is analyzed here. The simulations show that the time-averaged meridional transport of turbulence (and the expected sediment transport) is from the inlets to the north and from the open boundary to the south. In the tidal

basins this transport is southward, giving theoretical support to the observed accumulation of sediment on the flats. The weak level of tidally driven turbulence along the northern coasts of the barrier islands and the small magnitude of the residual currents there contribute to an accumulation of suspended particles in these areas.

One advantage of the simulations with respect to the limited amount of existing observations is their ability to provide estimates about some circulation characteristics which are difficult to reconstruct from spot observations. One such characteristic is the transport between the basins. We demonstrated in this paper that in the absence of wind this transport is much smaller than the transport through the inlets. The water accumulated in the flat areas, which is due to the interbasin exchange, and the water which is transported through inlets show quite a complicated correlation, thus revealing the large sensitivity of interbasin exchange to small differences in the model forcing. Obviously, this issue deserves further analysis with models forced by realistic winds to account for meteorological impacts.

Acknowledgements We are indebted to S. Dick for providing the data from the operational model of BSH and to B. Flemming for the useful discussions. The topography data and Fig. 1 have been prepared in cooperation with F. Meyer. Figure 2 has been prepared by G. Brink-Spalink. We also thank for the comments from an anonymous reviewer which helped to improve our paper.

References

Antia EE (1993) Sedimentology, morphodynamics and facies association of a mesotidal barrier and island shoreface (Spiekeroog, Southern North Sea). Berichte aus dem Fachbereich Geowissenshaften der Universität Bremen 32: 370 pp

Arakawa A, Lamb VR (1977) Computational design of the basic dynamical processes of the UCLA general circulation model. Meth Computat Phys 16: 173–263

Aubrey DG, Speer PE (1985) A study of non-linear tidal propagation in shallow inlet/estuarine systems. Part I: Observations. Estuarine Coastal Shelf Sci 21: 185–205

Backhaus JO (1983) A semi-implicit scheme for the shallow water equations for application to shelf sea modeling. Cont Shelf Res 4: 243–254

Beckers J-M, Deleersnijder E (1993) Stability of a FBTCS scheme applied to the propagation of shallow-water inertia-gravity waves on various space grids. J Comput Phys 108: 95–104

Boon JD III, Byrne RJ (1981) On the basin hypsometry and the morphodynamic response of coastal inlet systems. Mar Geol 40: 27–48

Bruun P (1978) Stability of tidal inlets. Theory and engineering. Developments in geotechnical engineering 23, Elsevier, Amsterdam, 506 pp

Burchard H (1998) Presentation of a new numerical model for turbulent flow in estuaries and Wadden seas. In: Babovic V and Larsen LC (eds) Hydroinformatics '98. Proceedings of the Third International Conference on Hydroinformatics, Copenhagen, Denmark, 24–26 August 1998, Balkema, Rotterdam, 41–48

Burchard H, Bolding K (2002) GETM – a general estuarine transport model. Scientific Documentation, No EUR 20253 EN, European Commission, printed in Italy, 157 pp

Burchard H, Petersen O (1997) Models of turbulence in the marine environment – a comparative study of two-equation turbulance models. J Mar Syst 21: 29–53

Davis RA Jr, Flemming B (1991) Time-series study of mesoscale tidal bedforms, Martens Plate, Wadden Sea, Germany. In: Smith DG, Reinson GE, Zaitlin BA, Rahmani RA (eds) Clastic Tidal Sedimentology, Canadian Society of Petroleum Geologists. Memoir 16: 275–282

de Kok JM (2002) The influence of freshwater distribution on SPM transport in the Dutch coastal zone. In: Winterwerp J, Kranenburg C (eds) Fine sediment dynamics in the marine environment. Elsevier, Amsterdam, pp 563–576

Dick SK, Sötje K (1990) Ein operationelles Ölausbreitungsmodell für die deutsche Bucht. Dt Hydrogr Z, Ergänzungsheft (A) 16: 243–254

Dick S, Schönfeld W (1996) Water transport and mixing in the North Frisian Wadden Sea. Results of numerical investigations. Dt Hydrogr Z 48: 27–48

Dick SK, Eckhard K, Müller-Navarra SH, Klein H, Komo H (2001) The operational circulation model of BSH (BSHcmod) – model description and validation. Berichte des BSH: 29, 49 pp

Dittmann S (1999) The Wadden Sea ecosystem: stability, properties and mechanisms. Springer, Berlin Heidelberg, New York, 299 pp

Ferk U (1995) Folgen eines beschleunigten Meeresspiegelanstiegs für die Wattengebiete der niedersächsischen Nordseeküste. Die Küste. Archiv für Forschung und Technik an der Nord und Ostsee 57: 135–156

Fitzgerald DM, Nummedal D (1988) Response characteristics of an ebb-dominated tidal inlet channel. J Sedim Petrol 27: 521–545

Flemming BW, Davis RA (1994) Holocene evolution, morphodynamics and sedimentology of the Spiekeroog barrier island system (southern North Sea). Senkenbergiana Maritima 24: 117–155

Friedrichs CT, Aubrey DG (1988) Nonlinear tidal distortion in shallow well-mixed estuaries: a synthesis. Estuarine Coastal Shelf Sci 26: 521–545

Hayes M (1979) Barrier island morphology as a function of tidal and wave regime. In: Leatherman SP (ed) Barrier Islands from the Gulf of St. Lawrence to the Gulf of Mexico. Academic Press, New York, pp 1–29

Hübner U, Backhaus JO (1997) Der küstennahe Gezeitenstrom im Gebiet der Östlichen Ostfriesischen Inseln. Forschungszent Terramare, Ber 4: 65 pp

Huthnance JM (1973) Tidal current asymmetries over Norfolk Sandbanks. Estuarine Coastal Mar Sci 1: 89–99

Jay D, Smith JD (1988) Residual circulation in and classification of shallow stratified estuaries. In: Dronkers J, van Leussen W (eds) Physical processes in estuaries, Springer, Berlin, Heidelberg, New York, pp 21–44

Kagan B (1995) Ocean–atmosphere interaction and climate modelling. Cambridge University Press, Cambridge, 391 pp

Keulegan GH (1967) Tidal flow in entrances: water level fluctuations of basins in communication with the seas. Committee on Tidal Hydraulics Technical Bulletin 14, US Army Engineers Waterways Experiment Station, Vicksburg, MS

Lassen H (1989) Örtliche und zeitliche Variationen des Meeresspiegels in der südöstlichen Nordsee. Die Küste. Archiv für Forschung und Technik an der Nord und Ostsee, 50: 65–96

Lassen H, Siefert W (1991) Mittlere Tidewasserstände in der Südöstlichen Nordsee – säkularer Trend und Verhältnisse um 1980. Die Küste. Archiv für Forschung und Technik an der Nord-und Ostsee, Heft 52: 85–137

Lighthill J (1978) Waves in fluids. Cambridge University Press, Cambridge, 520 pp

Maas LRM (1998) On an oscillator equation for tides in almost enclosed basins of non-uniform depth. In: Physics of estuaries and coastal seas. Dronkers J, Scheffers M (eds) Balkema, Rotterdam, pp 127–132

Mehta AJ (1978) Inlet hydraulics. Flow dynamics and nearshore transport. In: Stability of tidal inlets. Theory and engineering. Development in geotechnical engineering 23, Elsevier, Amsterdam pp 83–161

Nyandwi N, Flemming B (1995) A hydraulic model for the shore-normal energy gradient in the East Frisian Wadden Sea (Southern North Sea). Senckenbergiana Maritima 25: 163–171

Otto L, Zimmerman JTF, Furnes GK, Mork M, Saertre R, Becker G (1990) Review of the physical oceanography of the North Sea. Neth J Sea Res 26: 161–238

Ridderinkhof H (1988) Tidal and residual flows in the Western Dutch Wadden Sea. I: Numerical model results. Neth J Sea Res 22: 1–21

Ridderinkhof H (1990) Tidal and residual flows in the Western Dutch Wadden Sea. III: Vorticity balances. Neth J Sea Res 24: 9–26, 1989

Ridderinkhof H, Zimmermann JTF (1990a) Resudual currents in the Western Dutch Wadden Sea. In: Cheng RT (ed) Coastal and estuarine studies. Springer, Berlin, Heidelberg, New York, pp 93–104

Ridderinkhof H Zimmermann JTF (1990b) Mixing procecess in a numerical model of the Western Dutch Wadden Sea. In: Cheng RT (ed) Coastal and estuarine studies. Springer, Berlin, Heidelberg, New York, pp 194–209

Rodi W (1980) Turbulence models and their application in hydraulics. Rep Int Assoc Hydraul Res, Delft, Netherlands, 104 pp

Santamarina Cueno P, Flemming B (2000) Quantifying the concentration and flux of suspended particulate matter through a tidal inlet of the East Frisian Wadden Sea by acoustic Doppler current profiling. In: Flemming BW, Delafontaine MT, Liebezeit G. (eds) Muddy coast dynamics and resource management. Elsevier Science, Amsterdam, pp 39–52

Trowbridge JH, Chapman DC, Candela J (1998) Topographic effects, straits and the bottom boundary layer. In: Brink KH, Robinson AR (eds) The sea, 10. pp 63–88

van der Ham R, Winterwerp JC (2001) Turbulent exchange of fine sediments in a tidal channel in the Ems/Dollard estuary. Part II. Analysis with a 1DV numerical model. Cont Shelf Res 21: 1629–1647